

THE DISK-OUTFLOW SYSTEM IN THE S255IR AREA OF HIGH MASS STAR FORMATION

I. ZINCHENKO^{1,2}, S.-Y. LIU³, Y.-N. SU³, S. V. SALII⁴, A. M. SOBOLEV⁴, P. ZEMLYANUKHA^{1,2}, H. BEUTHER⁵,
D. K. OJHA⁶, M. R. SAMAL⁷, Y. WANG^{8,9}

(Received receipt date; Revised revision date; Accepted acceptance date)

Draft version February 20, 2024

ABSTRACT

We report the results of our observations of the S255IR area with the SMA at 1.3 mm in the very extended configuration and at 0.8 mm in the compact configuration as well as with the IRAM-30m at 0.8 mm. The best achieved angular resolution is about 0.4 arcsec. The dust continuum emission and several tens of molecular spectral lines are observed. The majority of the lines is detected only towards the S255IR-SMA1 clump, which represents a rotating structure (probably disk) around the young massive star. The achieved angular resolution is still insufficient for conclusions about Keplerian or non-Keplerian character of the rotation. The temperature of the molecular gas reaches 130–180 K. The size of the clump is about 500 AU. The clump is strongly fragmented as follows from the low beam filling factor. The mass of the hot gas is significantly lower than the mass of the central star. A strong DCN emission near the center of the hot core most probably indicates a presence of a relatively cold ($\lesssim 80$ K) and rather massive clump there. High velocity emission is observed in the CO line as well as in lines of high density tracers HCN, HCO⁺, CS and other molecules. The outflow morphology obtained from combination of the SMA and IRAM-30m data is significantly different from that derived from the SMA data alone. The CO emission detected with the SMA traces only one boundary of the outflow. The outflow is most probably driven by jet bow shocks created by episodic ejections from the center. We detected a dense high velocity clump associated apparently with one of the bow shocks. The outflow strongly affects the chemical composition of the surrounding medium.

Subject headings: astrochemistry – HII regions – instrumentation: interferometers – ISM: clouds – ISM: molecules – stars: formation

1. INTRODUCTION

The formation of high mass stars (more massive than 8–10 M_⊙) is still poorly understood. Studies of this process are currently a “hot topic” of astrophysical research. A major unsolved problem of high mass star formation is the characterization of accretion disks around young high-mass protostars. To date, most of evidence for the existence of such disks has been indirect (e.g. Beuther et al. 2009). If present, these disks undoubtedly play a crucial role in the star formation process. Nevertheless, the very existence of these disks, much less their physical properties, is not well-established. The importance of understanding these disks cannot be understated. For example, because of the larger masses involved, it is quite possible that high-mass disks are self-gravitating, unlike their Keplerian low-mass counterparts, implying that

there may be significant dynamical differences between the high-mass and low-mass star formation processes.

S255IR is a part of the well known massive star forming complex located between the evolved Sharpless H II regions S255 and S257. Several authors estimated the photometric distance to the complex at about 2.5 kpc (Russeil et al. 2007; Chavarría et al. 2008; Ojha et al. 2011). However, Rygl et al. (2010) report a distance of 1.6 kpc based on trigonometric parallax measurements of methanol masers. This seems to be the most accurate distance estimate and we adopt it here, too. The previous studies have shown that S255IR contains a cluster of early-B-type stars (Howard et al. 1997; Itoh et al. 2001), several compact H II regions (Snell & Bally 1986), and a number of H₂ emission features (Miralles et al. 1997). The total mass of the S255IR core has been estimated from single-dish observations at $M \sim 300 - 400$ M_⊙ (Zinchenko et al. 2009; Wang et al. 2011). The estimate of the luminosity has been $L \sim 2 \times 10^4$ L_⊙ (Wang et al. 2011).

The interferometric observations by Wang et al. (2011) revealed 3 continuum clumps and a high-velocity collimated outflow in the S255IR area. Our Paper I (Zinchenko et al. 2012) was devoted to the general structure and kinematics of the complex based on the SMA observations at 1.3 and 1.1 mm (the synthesized beam sizes were approximately $3''.8 \times 3''.0$ at 1.3 mm and $2''.9 \times 2''.6$ at 1.1 mm) as well as VLA ammonia observations and GMRT low frequency continuum data. Our results as well as data by Wang et al. (2011) indicate in particular a presence of a hot rotating core and a spectacular outflow in the S255IR region. However the angular

zin@appl.sci-nnov.ru

¹ Institute of Applied Physics of the Russian Academy of Sciences, 46 Ulyanov st., Nizhny Novgorod 603950, Russia² Lobachevsky State University of Nizhny Novgorod, 23 Gagarin av., Nizhny Novgorod 603950, Russia³ Institute of Astronomy and Astrophysics, Academia Sinica, P.O. Box 23-141, Taipei 10617, Taiwan, R.O.C.⁴ Ural Federal University, Ekaterinburg, Russia⁵ Max-Planck-Institut für Astronomie, Heidelberg, Germany⁶ Infrared Astronomy Group, Department of Astronomy and Astrophysics, Tata Institute of Fundamental Research, Homi Bhabha Road, Colaba, Mumbai (Bombay) – 400 005, India⁷ Laboratoire d'Astrophysique de Marseille (UMR 6110 CNRS & Université de Provence), 38 rue F. Joliot-Curie, 13388 Marseille Cedex 13, France⁸ Department of Astronomy, University of Geneva, Switzerland⁹ Purple Mountain Observatory, CAS, China

resolution was insufficient for a more detailed investigation of this core. In addition, a reliable evaluation of physical and chemical properties of this system required observations of additional molecular transitions. Therefore we performed observations of the S255IR area with the SMA at a much higher angular resolution and at higher frequencies.

Here we present observational data for S255IR obtained at 1.3 mm with the SMA in the very extended configuration and at 0.8 mm in the compact configuration. In addition we observed this area with the IRAM 30m radio telescope in order to obtain short-spacing data complementing the SMA results. We mainly discuss properties of the dense cores and high velocity outflows observed in this area.

2. OBSERVATIONS AND DATA REDUCTION

2.1. SMA

The S255 IR area was observed with the Submillimeter Array (SMA) in its compact configuration on 2010 December 14th at 350 GHz. A three field mosaic was obtained with the following phase centers: $06^h12^m53^s.800$, $17^\circ59'22''.1$, $06^h12^m54^s.8876$, $17^\circ59'29''.3353$ and $06^h12^m52^s.7124$, $17^\circ59'14''.8647$. The primary HPBW of the SMA antennas is $36''$ at these frequencies. Typical system temperatures on source were between 200 K and 400 K. The resulting uv coverage ranges from 10 k λ to 90 k λ (8 antennas in the array). 3C454.3 and Uranus were used as the bandpass calibrators and 0532+075, 0750+125 and 0530+135 were used as the complex phase and amplitude gain calibrators. A total of 8 GHz (342–346 GHz in the LSB and 354–358 GHz in the USB) was observed with the SMA bandwidth doubling correlator configuration. The spectral resolution was 0.8125 MHz.

In addition on 2011 January 07th S255IR was observed in the very extended configuration at 225 GHz. A single field was observed with the same phase center as for the central field at 350 GHz. The primary HPBW of the SMA antennas is $55''$ at these frequencies. Typical system temperatures on source were between 90 K and 200 K. The resulting uv coverage ranges from 50 k λ to 350 k λ (7 antennas in the array). 3C454.3 and 3C279 were used as the bandpass calibrators and 0750+125 and 0530+135 were used as the complex phase and amplitude gain calibrators. A total of 8 GHz (217.0–220.8 GHz in the LSB and 229.1–232.95 GHz in the USB) was observed with the SMA bandwidth doubling correlator configuration. The spectral resolution was 0.406 MHz and 1.625 MHz (given the limited correlator capability, we were not able to have the high resolution across the whole band; so, we assigned different resolutions for different tracers). These data were combined with our previous data obtained at the same frequencies in the compact configuration (Paper I) which enables an investigation of the source structure in a wider range of spatial scales.

The gain calibrator flux scale, calibrated against Uranus at 350 GHz and Callisto at 225 GHz, was found to be consistent within 5% with the SMA calibrator database and estimated to be accurate within 20%.

The data calibration was carried out with the IDL superset MIR (Scoville et al. 1993), and subsequent imaging and analysis were done in MIRIAD (Sault et al.

1995). With robust weighting for the continuum and line data, the synthesized beam sizes are approximately $2''.2 \times 1''.9$ at 350 GHz and $0''.5 \times 0''.4$ at 225 GHz. The rms noise is approximately 7 mJy beam $^{-1}$ and 1 mJy beam $^{-1}$ in the continuum images at 350 GHz and 225 GHz, respectively, and 100 mJy beam $^{-1}$ and 20 mJy beam $^{-1}$ in the spectral cubes at these frequencies at 2 km s $^{-1}$ resolution.

2.2. IRAM 30m radio telescope

Single-dish observations of several molecular lines at the 30m IRAM radio telescope were performed in October 2012 (N_2H^+ $J = 3 - 2$ at 279.5 GHz), December 2012 (SiO $J = 5 - 4$ at 217.1 GHz) and January 2014 (CO $J = 3 - 2$ at 345.8 GHz and CS $J = 7 - 6$ at 342.9 GHz). The antenna HPBW was $9''.3$, $11''.9$ and $7''.5$ at these frequencies, respectively. The observations were performed in the OTF mode with position switching using the HERA receiver at 217.1 GHz and EMIR receiver at higher frequencies. The central position of the maps was the same as for the primary field in the SMA observations. The reference position was selected at $-500''$ in right ascension from the central position. Apparently a weak CO(3–2) emission is present at the reference position resulting in a weak negative feature in the CO spectra at $V_{\text{LSR}} \approx 24$ km s $^{-1}$ (the bulk of the line emission in this area is observed at $V_{\text{LSR}} \sim 4 - 10$ km s $^{-1}$). This feature does not affect significantly the observed spectra. The system temperature was ~ 200 K for the N_2H^+ observations, ~ 300 K for the SiO observations and ~ 600 K for the CO and CS observations. Pointing was checked regularly on nearby strong sources and pointing errors were within a few arcseconds. The antenna temperature calibration was made by the standard chopper-wheel method.

The map size was approximately $2'.0 \times 2'.5$ for the N_2H^+ and SiO observations, covering both S255IR and S255N regions, and approximately $1'.5 \times 1'.0$ for the CO and CS observations, covering only the S255IR area. Here we discuss only the data relevant to S255IR. The data on S255N are postponed for further publications.

The data reduction was performed with the GILDAS package (<http://www.iram.fr/IRAMFR/GILDAS>). Then the single-dish data were combined with the SMA data using the MIRIAD procedures as described by e.g. Wang et al. (2011). The conversion to the flux density scale was made using the conversion factors presented on the IRAM 30m telescope website.

3. OBSERVATIONAL RESULTS AND DATA ANALYSIS

With the SMA we detected several tens of spectral lines in both 350 GHz and 225 GHz bands. A list of these lines, including their frequencies and energy of lower levels, is given in Tables 1, 2. The spectral line parameters are taken from the JPL (Pickett et al. 1998) and CDMS (Müller et al. 2001, 2005) catalogs.

We present the results in the form of maps as well as spectra and line parameters at selected positions. For continuum observations we give positions, flux densities, and size estimates of the continuum sources.

3.1. Data analysis

3.1.1. Methanol

Table 1

List of molecular transitions observed at the SMA in the very extended configuration in S255IR.

Molecule	Transition	Frequency (GHz)	E_l (K)
^{12}CO	2–1	230.538000	5.532
^{13}CO	2–1	220.398684	5.289
CH_3OH	6 ₁ – 7 ₂ A [–]	217.299202	363.496
	15 ₆ – 16 ₅ A [–]	217.642677	735.160
	15 ₆ – 16 ₅ A ⁺	217.642678	735.160
	20 ₁ – 20 ₀ E	217.886504	497.919
	4 ₂ – 3 ₁ E	218.440063	34.976
	8 ₀ – 7 ₁ E	220.078561	86.051
	15 ₄ – 16 ₃ E	229.589056	363.420
	8 _{–1} – 7 ₀ E	229.758756	78.076
	19 ₅ – 20 ₄ A ⁺	229.864121	567.565
	19 ₅ – 20 ₄ A [–]	229.939095	567.561
	3 _{–2} – 4 _{–1} E	230.027047	28.788
	22 ₂ – 21 _{–3} E	230.292196	598.499
	10 ₂ – 9 ₃ A [–]	231.281110	154.248
	10 ₂ – 9 ₃ A ⁺	232.418521	154.248
	18 ₃ – 17 ₄ A ⁺	232.783446	435.360
^{13}CS	5–4	231.220686	22.194
DCN	3–2	217.238530	10.425
HNCO	10 _{0,10} – 9 _{0,9}	219.798282	47.471
	10 _{1,9} – 9 _{1,8}	220.584762	90.916
	10 _{1,10} – 9 _{1,9}	218.981170	90.569
	10 _{2,9} – 9 _{2,8}	219.733850	217.739
	10 _{2,8} – 9 _{2,7}	219.737193	217.739
	10 _{3,8} – 9 _{3,7}	219.656770	422.417
	10 _{3,7} – 9 _{3,6}	219.656771	422.417
HC_3N	24–23	218.324711	120.504
SO	6 ₅ – 5 ₄	219.949433	24.429
H_2CO	30 _{,3} – 20 _{,2}	218.222195	10.483
	32 _{,2} – 22 _{,1}	218.475642	57.608
	32 _{,1} – 22 _{,0}	218.760071	57.613
OCS	18–17	218.903357	89.304
	19–18	231.060983	99.810
HCOOH	10 _{0,10} – 9 _{0,9}	220.038072	48.061
	10 _{1,9} – 9 _{1,8}	231.505705	53.355
CH_3CN	12 ₆ – 11 ₆	220.594423	315.313
	12 ₅ – 11 ₅	220.641084	236.810
	12 ₄ – 11 ₄	220.679287	172.555
	12 ₃ – 11 ₃	220.709017	122.565
	12 ₂ – 11 ₂	220.730261	86.849
	12 ₁ – 11 ₁	220.743011	65.416
	12 ₀ – 11 ₀	220.747261	58.272

For the methanol data analysis, we constructed simple radiative transfer model, which uses the large velocity gradient (LVG) approximation. Dust emission and absorption within the emission region was taken into account in the way described by Sutton et al. (2004). We assumed that the dust particles are intermixed with gas. The same physical temperature for the gas and dust components is assumed. The molecular emission region was assumed to be spherically symmetric and uniform in H_2 density, gas and dust temperature, gas-to-dust ratio and methanol fractional abundance. The influence of external infrared sources was not considered. The dust opacity law was chosen as $\tau_{\text{dust}} \propto \lambda^{-2}$. We adopted a gas-to-dust mass ratio of 100 and a cross section at 1 mm of $2.6 \times 10^{-25} \text{ cm}^2$ (Sherwood et al. 1980). In addition to the model described in Sutton et al. (2004) we used the collision transition rates based on the model of collisions of methanol molecules with He and para- H_2 molecules (Cragg et al. 2005). Scheme of energy levels in this model includes rotational levels with the quantum numbers J up to 22, $|K|$ up to 9; the levels include the rotational levels of the ground, first and second torsionally excited

Table 2

List of molecular transitions observed at the SMA in the compact configuration in S255IR.

Molecule	Transition	Frequency (GHz)	E_l (K)
^{12}CO	3–2	345.795990	16.596
CS	7–6	342.882850	49.372
HCO^+	4 – 3	356.734242	25.682
CH_3OH	13 ₁ – 13 ₀ A [–] +	342.729796	211.024
	13 _{–1} – 14 _{–2} E	343.599019	607.550
	18 ₂ – 17 ₃ E	344.109039	402.884
	19 ₁ – 18 ₂ A ⁺	344.443433	434.697
	16 ₁ – 15 ₂ A [–]	345.903916	316.049
	18 _{–3} – 17 _{–4} E	345.919260	442.829
	13 ₀ – 12 ₁ A ⁺	355.602945	193.959
HCN	4–3	354.505473	25.251
	4–3 (0,1 ^{1c} ,0)	354.460435	1049.892
	4–3 (0,1 ^{1d} ,0)	356.255568	1050.021
H^{13}CN	4–3	345.339769	24.861
HC^{15}N	4–3	344.200109	24.779
HC_3N	38–37	345.609016	306.905
	39–38	354.697456	323.492
SO	8 ₈ – 7 ₇	344.310792	70.957
^{33}SO	8 _{9,8} – 7 _{8,7}	343.086102	61.564
	8 _{9,9} – 7 _{8,8}	343.087298	61.566
SO_2	13 _{2,12} – 12 _{1,11}	345.338538	76.410
	12 _{4,8} – 12 _{3,9}	355.045517	93.960
	13 _{4,10} – 13 _{3,11}	357.165390	105.823
	15 _{4,12} – 15 _{3,13}	357.241193	132.537
	11 _{4,8} – 11 _{3,9}	357.387580	82.800
	8 _{4,4} – 8 _{3,5}	357.581449	55.202
	9 _{4,6} – 9 _{3,7}	357.671821	15.992
	7 _{4,4} – 7 _{3,5}	357.892442	47.835
	6 _{4,2} – 6 _{3,3}	357.925848	41.402
H_2CS	17 _{4,14} – 17 _{3,15}	357.962905	162.932
	10 _{0,10} – 9 _{0,9}	342.946424	74.132
	10 _{2,9} – 9 _{2,8}	343.322082	126.830
	10 _{3,8} – 9 _{3,7}	343.409963	192.613
	10 _{3,7} – 9 _{3,6}	343.414146	192.556
HCOOH	16 _{1,16} – 15 _{1,15}	342.521225	127.153
	15 _{1,14} – 14 _{1,13}	343.952413	119.774
	16 _{0,16} – 15 _{0,15}	345.030596	126.494
	16 _{2,15} – 15 _{2,14}	356.137250	141.578

states. In total, 861 levels of A-methanol and 852 levels of E-methanol were considered according to Cragg et al. (2005).

With this model we made estimates of the hydrogen number density, n_{H_2} , specific column density of methanol, $N_{\text{CH}_3\text{OH}}/\Delta V$, gas kinetic temperature, T_{kin} and fractional abundance of methanol $N_{\text{CH}_3\text{OH}}/N_{\text{H}_2}$, using the measured values of “quasi-thermal” (i.e. non-maser) methanol lines. The variable parameter of the source size is introduced in order to take into account beam-dilution effects.

The brightness temperatures of all detected “quasi-thermal” methanol lines as well as upper limits for the brightness temperatures of other lines were taken into account.

We have searched for a set of parameters which provides the best agreement between the values of the calculated brightness temperatures (T_i^{mod}) and the measured brightness temperatures (T_i^{obs}). This corresponds to the minimum of $\chi^2 = \sum_i^N ((T_i^{\text{obs}} - T_i^{\text{mod}})/\sigma_i)^2$, where σ_i is observational uncertainty for a particular line.

The sources appear inhomogeneous in some cases. However, the LVG approximation treats the problem locally and does not actually require physical homogeneity of the source. It can be well used for inhomogeneous

medium (e.g. Ossenkopf 1997). We have chosen the simplest approximation for the case of the source which is smaller than the beam – introduced filling factor which is equal to the portion of the source size in the beam. The value of the filling factor is well constrained because the model is sensitive to its changes. We do not have enough observational constraints to study real clumpiness of the source. Introducing additional poorly constrained parameters will reduce validity of the modelling.

3.1.2. Methyl cyanide

Methyl cyanide (CH_3CN) is a symmetric-top molecule which is an efficient “thermometer” for dense molecular gas (e.g. Boucher et al. 1980). To derive the kinetic temperature we used the population diagram analysis which takes into account the optical depth in the CH_3CN lines and the beam filling factor as described by Wang et al. (2010).

3.2. Millimeter wave continuum

Maps of the continuum emission at 0.8 and 1.3 mm are presented in Fig. 1. The 1.3 mm map was obtained by combining our new measurements in the very extended configuration with the previous measurements in the compact configuration (Paper I). It shows a rather extended emission and compact cores in the SMA1 and SMA2 clumps.

Estimates of the continuum source parameters are given in Tables 3,4. For the measurements at 1.3 mm we indicate the parameters of the compact cores seen in the very extended configuration. Parameters of the more extended components were presented in Paper I. The measured fluxes are several hundreds mJy at 350 GHz and several tens mJy at 225 GHz in the very extended configuration. The deconvolved sizes are from ~ 1 arcsecond to a few arcseconds at 345 GHz and about 0.3 arcsecond for the compact cores at 225 GHz.

3.3. Basic properties of the molecular emission

Here we give the general description of the observed molecular emission. A more detailed information on the relevant species and transitions is presented in the following sections.

The general morphology and kinematics of the molecular emission was described in Paper I. Our new data set contains several tens of molecular transitions. In Fig. 2 we present representative maps obtained with the SMA at 0.8 mm.

These maps confirm that SMA1 is the brightest source of molecular emission in this area. High-excitation lines are observed exclusively towards this clump. Several lower excitation molecular lines are detected also in SMA2. Emission of HCN, SO and CH_3OH is observed also in SMA4. HCN and CS emission is probably present in the area to the west of SMA2, designated as S255IR- $\text{N}_2\text{H}^+(1)$ in Paper I. Since it is observed not in N_2H^+ only and for simplicity we shall designate it hereafter as SMA2-W.

A new feature, not noticed in our Paper I and in other previous works is a molecular clump to the east of SMA1 with a rather strong emission in the HCN, HCO^+ , CS and SO lines (Fig. 2). We shall designate it as SMA1-E. This clump is located near the head of the jet observed in the NIR emission (see below).

Spectra of several representative transitions towards the SMA1 and SMA2 clumps are presented in Figs. 3,4.

As mentioned in Paper I the main emission peak toward the SMA1 clump is at $V_{\text{LSR}} \sim 4 - 5 \text{ km s}^{-1}$. The line width is $\gtrsim 5 \text{ km s}^{-1}$. Several lines including CO, HCN, HCO^+ , CS, SO show broad wings indicative of high velocity outflow. We discuss this feature in the following sections. A rather strong emission is detected from vibrationally excited HCN with the excitation energy $\sim 1000 \text{ K}$ above the ground level.

The line emission from the SMA1-E clump peaks at about 8 km s^{-1} . The linewidth is large, $\sim 5 \text{ km s}^{-1}$.

The emission from the SMA2 clump is observed at about 10 km s^{-1} . The lines are narrow, $\sim 2 \text{ km s}^{-1}$.

With the very extended array we detected the line emission almost exclusively from the SMA1 compact core. No emission was detected in C^{18}O and SiO indicating an absence of compact structures in the lines of these molecules. The results of these observations are presented and discussed below.

4. STRUCTURE, KINEMATICS AND PHYSICAL PROPERTIES OF DENSE CORES

Our data presented in Paper I and here as well as data by Wang et al. (2011) indicate the presence of four continuum clumps in the S255IR area, designated from S255IR-SMA1 to S255IR-SMA4. In addition, in Paper I we detected clumps with a rather strong molecular emission without continuum counterpart in the SMA data. One of them, S255IR- $\text{N}_2\text{H}^+(1)$, is located close to SMA2 and was observed in the N_2H^+ , NH_3 and several CH_3OH lines. Estimates of their basic physical properties were presented in Paper I. Here we investigate further these objects using the new data set.

4.1. SMA1

SMA1 is the brightest object in this area. As shown in Sect. 3 most of the observed molecular lines are detected only here. The deconvolved size of the continuum source at 350 GHz measured with the SMA in the compact configuration (Table 3) is close to that found in Paper I. The flux density measured at 350 GHz is only slightly higher than the flux density obtained at 284 GHz (Paper I). It is worth noting that in Paper I we could not separate the SMA1 and SMA3 clumps. However, even if we take the integrated flux of these clumps at 350 GHz, the spectral index in the range 284–350 GHz will be only 1.6 which is inconsistent with a presumably optically thin dust emission at these frequencies. Most probably this implies a significantly larger flux loss at 350 GHz in comparison with the measurements at 284 GHz due to a smaller beam size.

The deconvolved size of the continuum source detected with the SMA in the very extended configuration is about $0''.3$ (Table 4) which corresponds to about 500 AU. The observed aspect ratio for this core is close to unity.

4.1.1. Kinematics

Wang et al. (2011) noticed rotation of the core around the axis roughly parallel to the outflow direction. Now, at sub-arcsecond resolution we can investigate the core kinematics on smaller scales. In Fig. 5 we present maps of the first moment of the CH_3OH emission in the $4_2 - 3_1$ E line and CH_3CN emission in the $12_3 - 11_3$ line. In this

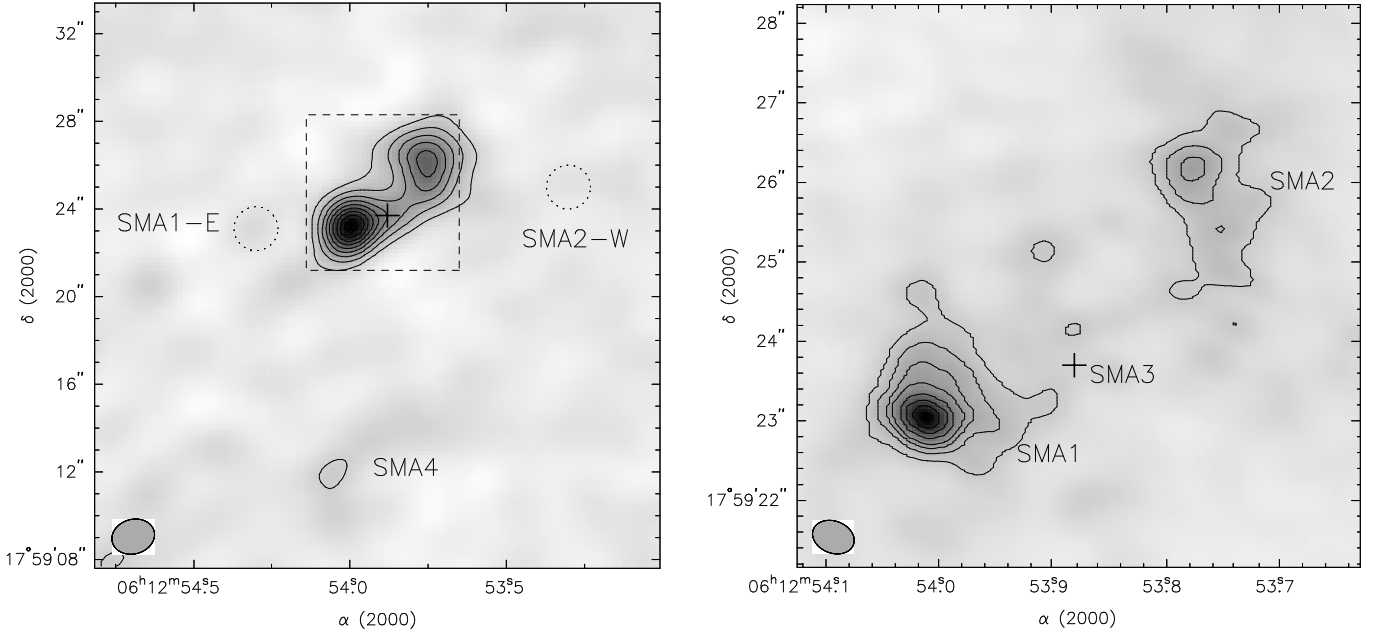


Figure 1. Lef panel: map of the 0.8 mm continuum emission in the S255IR. The contour levels are $(1, 2, 3, 4, 5, 6, 7, 8, 9, 10) \times 40 \text{ mJy beam}^{-1}$. The dashed rectangle indicates the area shown in the right panel. The dotted circles indicate positions of two molecular clumps discussed in the text. Right panel: map of the 1.3 mm continuum emission in the S255IR. The contour levels are $(2, 3, 4, 5, 7, 9, 11, 13) \times 4 \text{ mJy beam}^{-1}$. The SMA beam is shown in the lower left corner of both panels. The crosses mark the position of the SMA3 clump according to Wang et al. (2011).

Table 3

Names, positions, flux densities, deconvolved angular sizes and position angles of the millimeter wave continuum sources measured at 350 GHz in the compact configuration.

Name	$\alpha(2000)$ (h m s)	$\delta(2000)$ ($^{\circ}$ ' ")	S_{350} (Jy)	θ_{\max} (")	θ_{\min} (")	P.A. ($^{\circ}$)
S255IR-SMA1	6:12:54.00	17:59:23.2	0.50	1.4	0.6	-11
S255IR-SMA2	6:12:53.76	17:59:26.1	0.56	2.4	2.1	4
S255IR-SMA3	6:12:53.86	17:59:23.7	0.13	1.3	0.3	44
S255IR-SMA4	6:12:54.01	17:59:12.0	0.25	5.9	3.8	-82

Table 4

Names, positions, flux densities, deconvolved angular sizes and position angles of the millimeter wave continuum sources measured at 225 GHz in the very extended configuration.

Name	$\alpha(2000)$ (h m s)	$\delta(2000)$ ($^{\circ}$ ' ")	S_{225} (Jy)	θ_{\max} (")	θ_{\min} (")	P.A. ($^{\circ}$)
S255IR-SMA1	6:12:54.010	17:59:23.06	0.058	0.30	0.27	-19
S255IR-SMA2	6:12:53.779	17:59:26.16	0.016	0.49	0.31	-27

figure we also indicate the axis of the jet previously identified through IR observations (Howard et al. 1997) and locations of the water masers measured with the VLBA (Goddi et al. 2007).

This figure clearly shows that the core is really rotating around the axis of the jet. The rotation velocities along the line of sight amount to a few km s^{-1} (it varies from about 3 km s^{-1} to about 7 km s^{-1} for $\text{CH}_3\text{OH } 4_2 - 3_1 \text{ E}$ and to about 8 km s^{-1} for $\text{CH}_3\text{CN } 12_3 - 11_3$). In Fig. 6 we present the position-velocity diagram for the CH_3OH emission in the $4_2 - 3_1 \text{ E}$ line along the cut through the core center perpendicular to the jet axis ($\text{PA} = 157^{\circ}$). It clearly shows the velocity gradient which can be consis-

tent with Keplerian rotation but the angular resolution is still insufficient for firm conclusions about the character of this rotation.

An implicit indication of a probable further increase of the rotation velocity in the innermost part of the core comes from the line width map (Fig. 7). It shows a significant increase of the line width in the center which can be related to rotation (the line width increases from about 2 km s^{-1} at the periphery to about 6 km s^{-1} in the center).

It is also worth mentioning an increased line width along the jet axis (Fig. 7). It can be probably explained by an increased turbulence caused by the passage of the

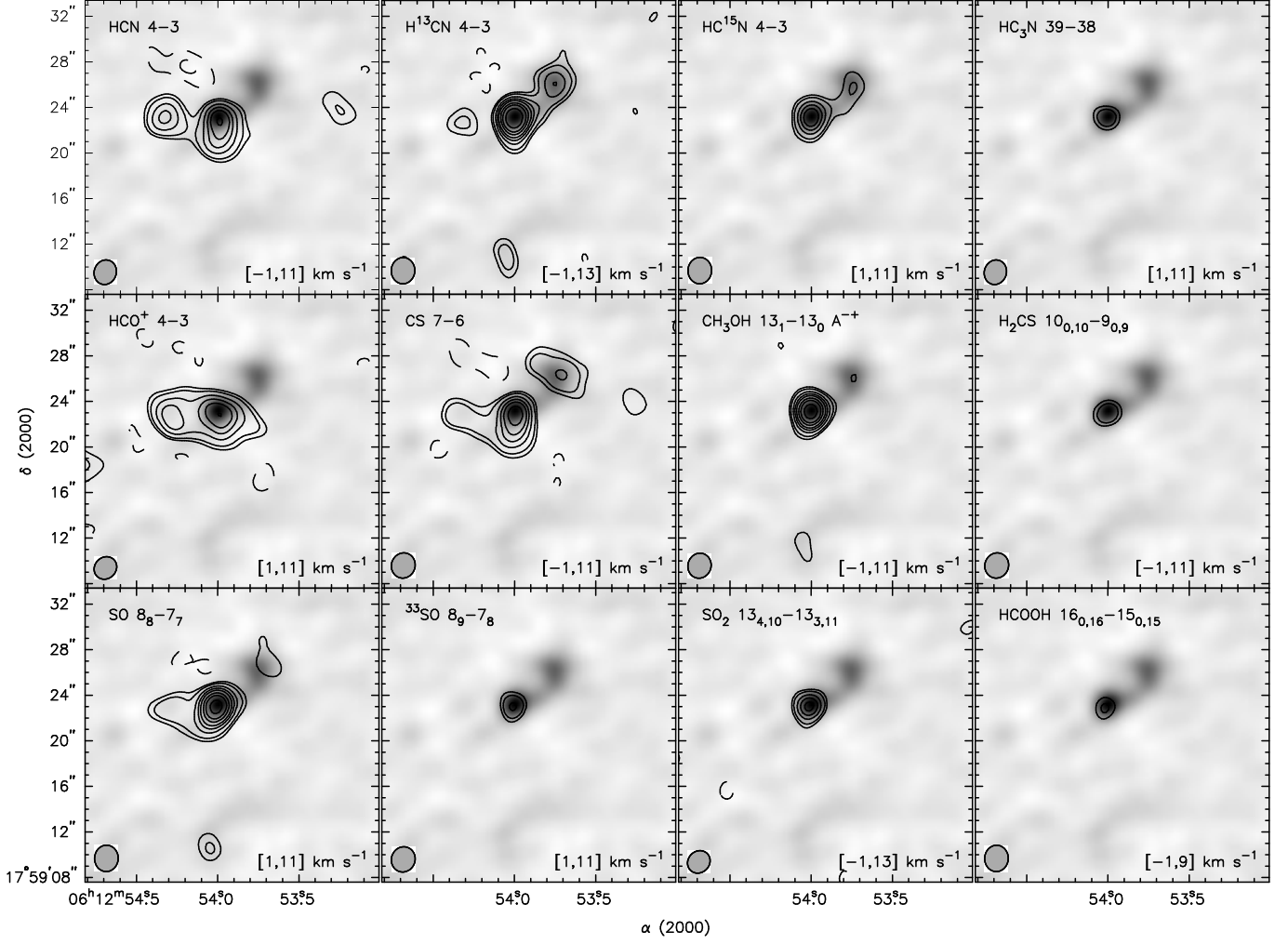


Figure 2. Maps of the integrated line emission for several representative transitions of various molecules (contours) overlaid on the image of the 0.8 mm continuum emission. The velocity interval is shown at the bottom of each panel. The dashed contours show negative features due to the missing flux. The contour levels are the following: $(-3, -2, 2, 3, 5, 7, 9, 12, 15, 20) \times A$ Jy beam $^{-1}$ km s $^{-1}$, where $A = 3$ for HCN and HCO $^{+}$, $A = 1$ for H 13 CN, HC 15 N, HC $_3$ N, H $_2$ CS, CH $_3$ OH, 33 SO, SO $_2$, and HCOOH, $A = 2$ for CS, and $A = 1.5$ for SO. The SMA beam is shown in the lower left corner of each panel.

jet.

The HCO $^{+}$ (4-3) and probably HCN(4-3) spectra towards SMA1 (Fig. 3) show the red-shifted absorption dip which may be suggestive of infall. The CO(3-2) spectrum measured with the SMA has a similar (although broader) feature (Fig. 8). At the same time the CO(3-2) spectrum obtained from the combined SMA and IRAM-30m data shows a peak at these velocities. Most probably it means that this feature is related to an extended component resolved out by the SMA, although an infall cannot be fully excluded.

4.1.2. Physical properties

Let us consider physical parameters of this core. We estimated gas kinetic temperature from the CH $_3$ CN and CH $_3$ OH observations. Modeling of the CH $_3$ CN emission (Fig. 9) as described in Sect. 3.1.2 yields kinetic temperature in the range (74.9 – 197.6) K (1σ confidence interval) towards the emission peak (Table 5). We have detected a large number (15) of CH $_3$ OH transitions towards SMA1 (Table 1). From the CH $_3$ OH analysis (Sect. 3.1.1) we obtain $T_{\text{kin}} = 178$ K with the 165 – 195 K 1σ confidence interval at the center, $T_{\text{kin}} = 170 - 200$ K at $0''.2$ to the

Table 5

Kinetic temperature, CH $_3$ CN column density, beam filling factor and line optical depth derived from the CH $_3$ CN data obtained in the very extended configuration (HPBW $\approx 0''.4$) at the central position in SMA1. The 1σ confidence intervals are indicated in the parentheses.

Parameter	Fit results
T_{kin} (K)	128.8 (74.9 – 197.6)
$N_{\text{L}}(\text{CH}_3\text{CN})$ (10^{16} cm $^{-2}$)	2.12 (0.96 – 5.80)
Beam filling factor	0.23 (0.18 – 0.36)
$\tau(K = 0)$	2.53 (0.93 – 8.37)

north and $T_{\text{kin}} = 140 - 165$ K at $0''.2$ to the south (Table 6). Therefore there is probably a temperature gradient in the north-south direction. The temperature seems to be anti-correlated with the CH $_3$ OH column density (Table 6).

We adopt the gas kinetic temperature of 170 K as the average value (it is close to the weighted average of the CH $_3$ OH and CH $_3$ CN results). Assuming the same temperature (170 K) for the dust we obtain a total mass

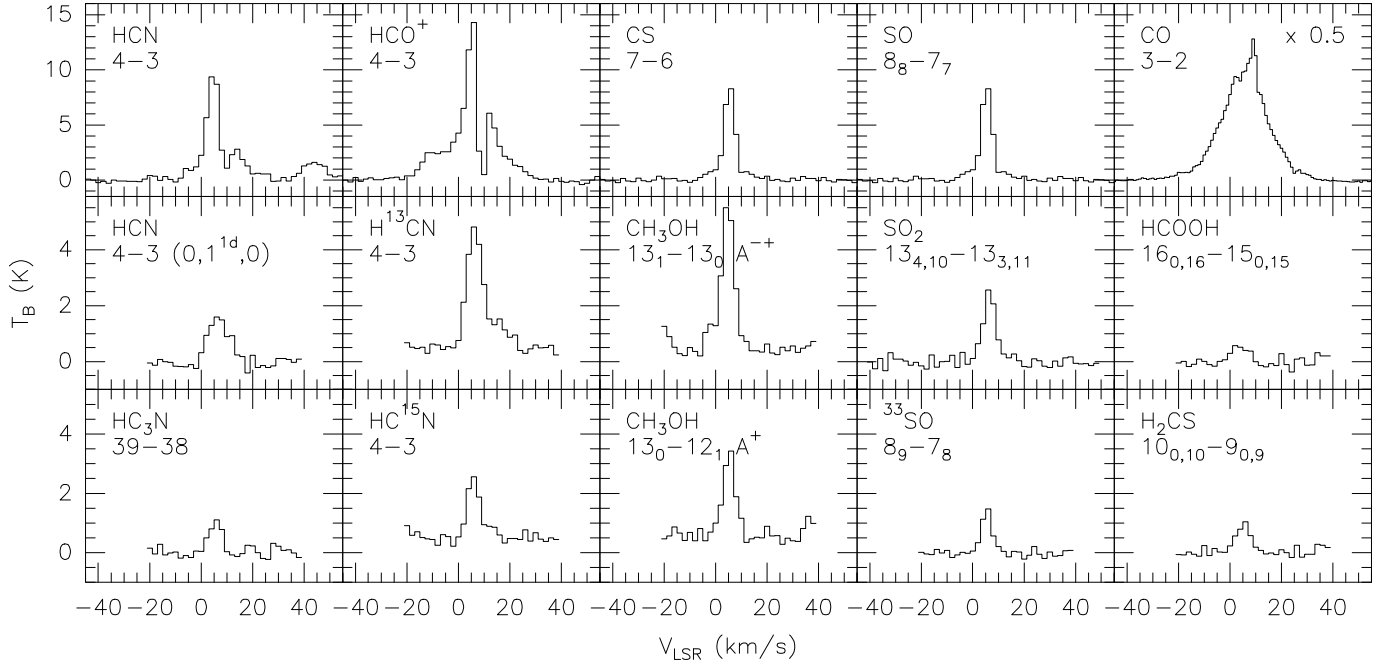


Figure 3. Spectra of several representative molecular transitions towards the SMA1 clump. The CO(3-2) spectrum is scaled by the factor of 0.5. It is obtained from the combined SMA and IRAM 30m data. The other spectra are from the SMA data only. The angular resolution is about 2 arcseconds.

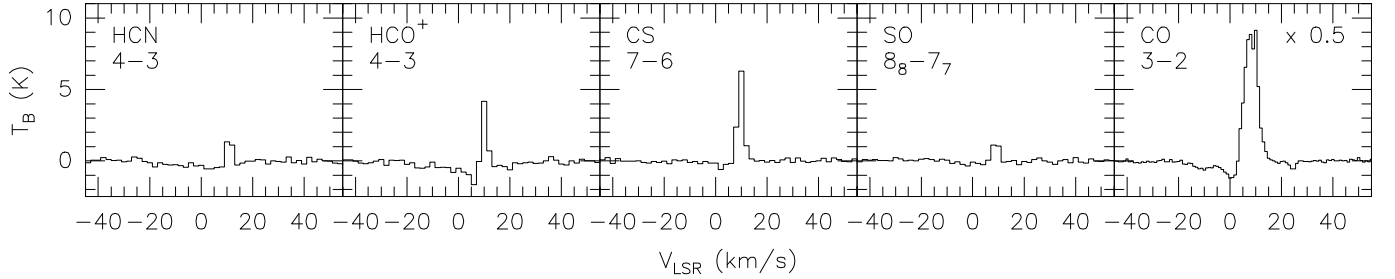


Figure 4. Spectra of several representative molecular transitions towards the SMA2 clump. The CO(3-2) spectrum is scaled by the factor of 0.5. It is obtained from the combined SMA and IRAM 30m data. The other spectra are from the SMA data only. The angular resolution is about 2 arcseconds.

Table 6

Physical parameters derived from the CH₃OH data obtained in the very extended configuration (HPBW $\approx 0''.4$) at several positions in SMA1. The 1σ confidence intervals are indicated in the parentheses (the density n_{H_2} is not constrained by the model as evident from Fig. 10).

Offsets ('', '')	T_{kin} (K)	$N_{\text{CH}_3\text{OH}}/\Delta V$ ($10^{12} \text{ cm}^{-3} \text{ s}$)	n_{H_2} (10^8 cm^{-3})	beam filling factor (%)	$N_{\text{CH}_3\text{OH}}/N_{\text{H}_2}$
0, +0.2	183 (170–200)	3.6 (2.8–5.0)	3.2	14.8 (13.9–16.4)	$10^{-6} (> 10^{-7})$
0, 0	178 (165–195)	5.6 (4.0–9.5)	3.2	16.0 (15.2–17.2)	$10^{-6} (> 10^{-7})$
0, -0.2	153 (140–165)	8.9 (5.0–12.6)	0.2	15.2 (13.3–16.0)	$10^{-6} (> 10^{-7})$

of this hot component of about $0.3 M_{\odot}$. As in Paper I we assume a gas-to-dust mass ratio of 100, and adopt a dust absorption efficiency following Ossenkopf & Henning (1994). The peak gas column density estimated from the continuum data is $N(\text{H}_2) \sim 3 \times 10^{24} \text{ cm}^{-2}$. With a size of 500 AU the mean density of hot gas is about $6 \times 10^8 \text{ cm}^{-3}$. This is 2 times higher than our estimate of the SMA1 mean density in Paper I taking into account the difference in the adopted distances here and in Paper I. This increase can be expected since now we consider much smaller scales near the core center. The CH₃OH modeling puts no significant constraints on den-

sity. The relative abundance of CH₃OH is $\sim 10^{-6}$.

Both CH₃CN and CH₃OH observations indicate beam filling factor of 0.15–0.2. This means that the source is very inhomogeneous on the $0''.4$ scale and probably consists of clumps with the size $\ll 500$ AU and density much higher than the mean density found above. This higher density estimate does not contradict the CH₃OH data. A similar picture of clumpy medium was inferred from our observations of high mass star forming regions on larger scales (Pirogov & Zinchenko 2008; Pirogov et al. 2012). Most probably it reflects turbulence in the cores.

Our data set includes several other tracers of the hot

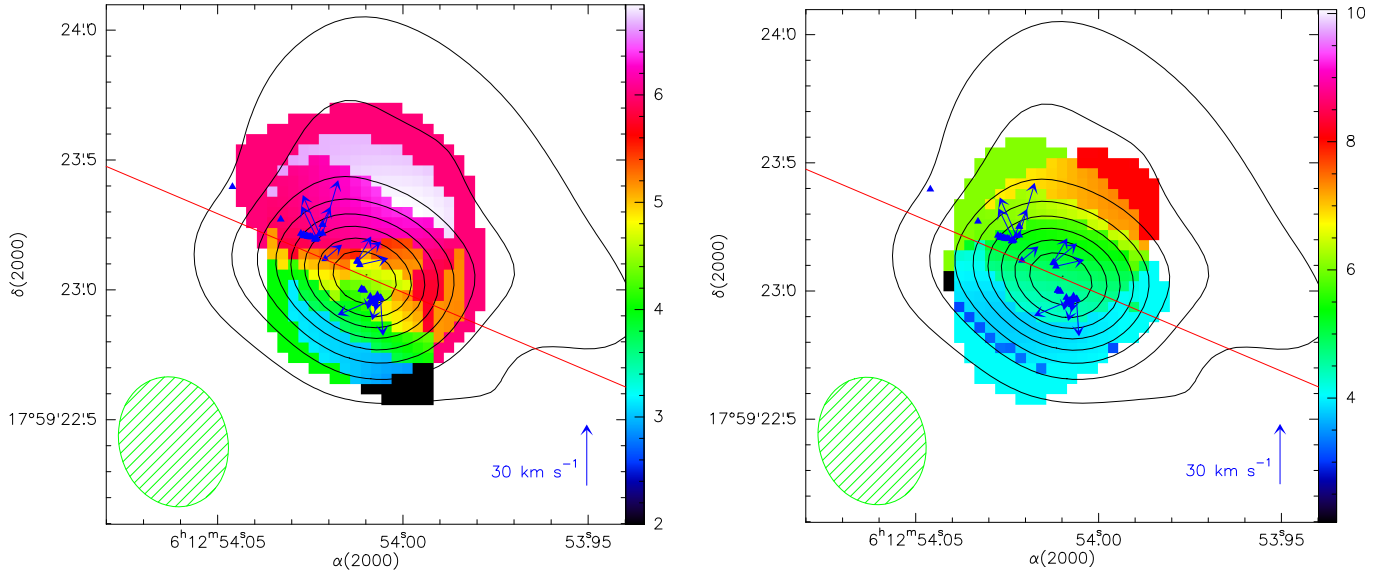


Figure 5. Maps of the first moment of the CH_3OH emission in the $4_2 - 3_1$ E line (left panel, color scale) and CH_3CN emission in the $12_3 - 11_3$ line (right panel, color scale) towards the SMA1 clump. The intensity cut-off is $100 \text{ mJy beam}^{-1} \text{ km s}^{-1}$ for CH_3OH and $200 \text{ mJy beam}^{-1} \text{ km s}^{-1}$ for CH_3CN . Contours show the 1.3 mm continuum emission. The triangles mark water masers (Goddi et al. 2007) and the arrows indicate their proper motions (in the cases when they are measured). The red line indicates the jet axis as found by Howard et al. (1997). The beam for the molecular maps is shown in the lower left corner of both panels. The scale for the velocities of the proper motions is shown in the lower right corner. The pixels with the lowest velocities appear as the blue squares in the right panel.

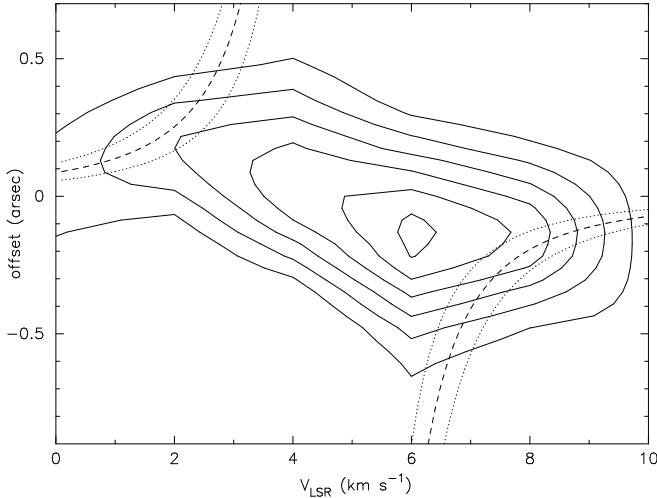


Figure 6. The position-velocity diagram for the CH_3OH emission in the $4_2 - 3_1$ E line along the cut through the SMA1 center perpendicular to the jet axis ($\text{PA} = 157^\circ$). The dashed curves correspond to Keplerian rotation around a central mass of $20 M_\odot$ with the inclination angle of 25° , the dotted curves correspond to the inclination angles of $25^\circ \pm 5^\circ$.

gas. One of the most important is HNC. We detected HNC lines in different K_{-1} ladders ($K_{-1} = 0, 1, 2, 3$) with the excitation energies up to $\sim 400 \text{ K}$ (Table 1). In Fig. 11 we present the rotational diagram for the observed HNC transitions. This diagram was obtained from peak integrated line intensities found by 2D Gaussian fitting of the integrated intensity maps in different HNC lines. We used the line strengths and dipole moment from the Cologne Database for Molecular Spectroscopy (Müller et al. 2001, 2005).

This diagram indicates a rotational temperature of $318 \pm 70 \text{ K}$ (Table 7). However, the $K_{-1} = 0, 1$ transitions can be saturated. The peak brightness temperature in these transitions is close to the brightness tempera-

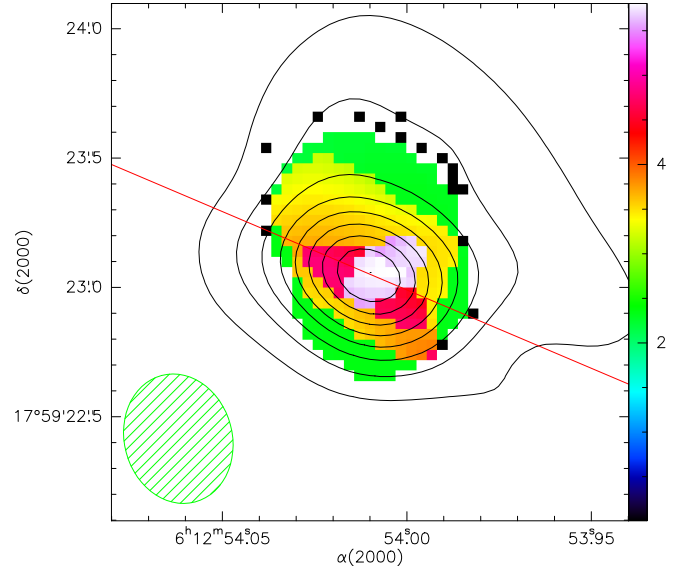


Figure 7. Map of the second moment of the CH_3OH emission in the $4_2 - 3_1$ E line (color scale). Contours show the 1.3 mm continuum emission. The beam for the molecular map is shown in the lower left corner.

ture in the apparently optically thick lines (e.g. CO and CH_3CN) and our modeling using RADEX (van der Tak et al. 2007) shows that at the derived physical parameters and column density the optical depth in these lines is about unity. In this case the derived rotational temperature would apparently represent an upper limit to the excitation temperature. The deconvolved source size is $\sim 0''.3 \times 0''.2$ for the $K_{-1} = 0$ transition and decreases for higher K_{-1} ladders. The map of the integrated intensity in the HNC $K_{-1} = 2$ transition is shown in Fig. 12 along with the map of the OCS emission which is another tracer of hot gas. The peaks of the HNC and OCS emission practically coincide with the continuum peak, although distributions of these molecules seem to

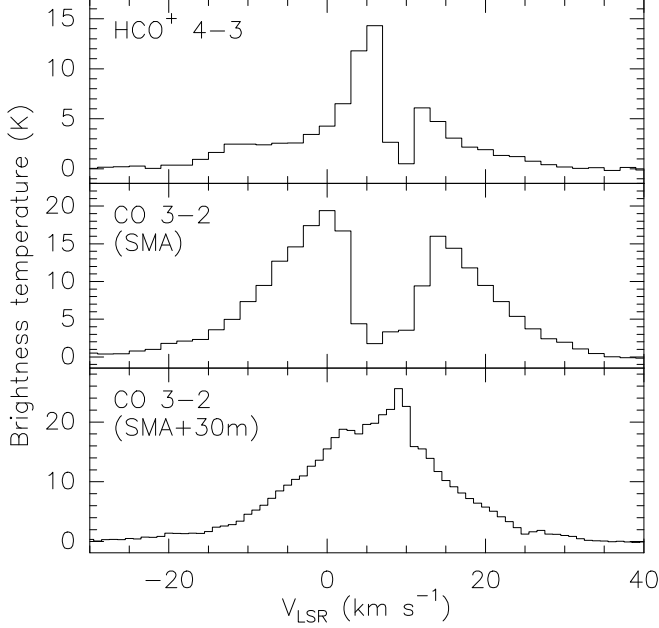


Figure 8. The SMA spectra of HCO^+ (4–3) and CO(3–2) as well as the combined SMA+30m spectrum of CO(3–2) towards SMA1. The angular resolution is about 2 arcseconds.

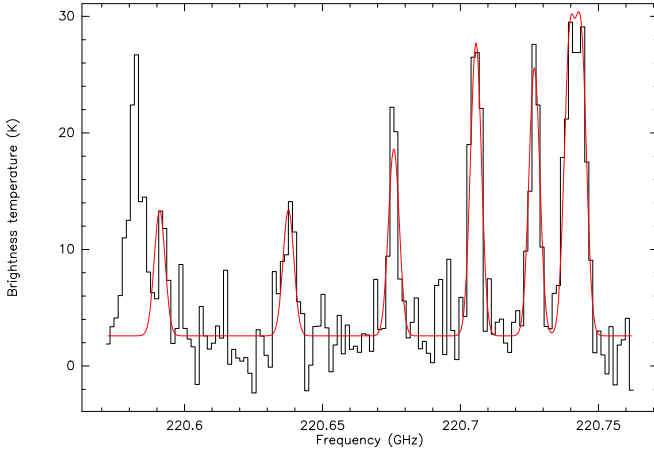


Figure 9. The CH_3CN spectrum measured towards the SMA1 emission peak and the model fit.

Table 7
Fit results for the rotational diagrams obtained towards SMA1. The 1σ uncertainties are indicated in the parentheses. In the last column the approximate HPBW for the corresponding data is indicated.

Molecule	T_{kin} (K)	$\log N_L$ (cm^{-2})	HPBW ($''$)
HNCO	318(70)	16.34(0.04)	≈ 0.4
SO ₂	146(16)	15.50(0.05)	≈ 2
	65(11)	15.35(0.08)	≈ 2

be somewhat different.

The total HNCO column density derived from the rotational diagram is $\sim 2 \times 10^{16} \text{ cm}^{-2}$. We used the partition function from the Cologne Database for Molecular Spectroscopy (Müller et al. 2001, 2005), too. A compar-

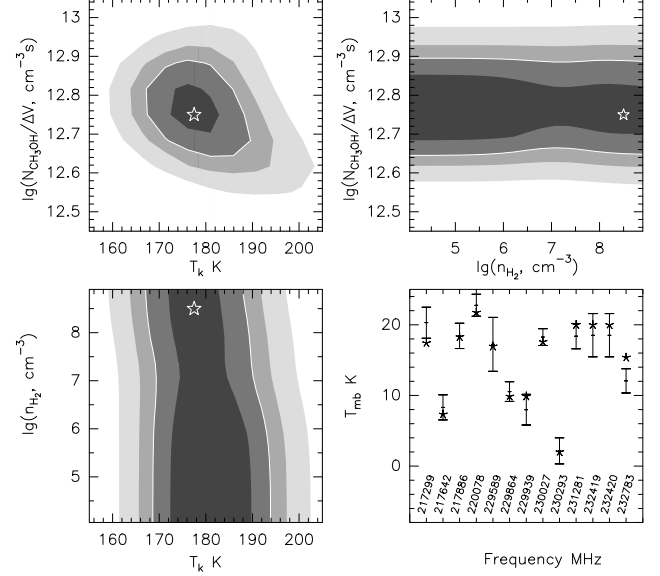


Figure 10. An example of the CH_3OH data fitting for the central position in SMA1. Variations of χ^2 with the model parameters are shown in the 2 top and left bottom panels. The minimum of χ^2 is marked by the star. Confidence intervals of 0.25, 1, 1.6 2.6 σ are plotted on the grey scale. The confidence interval of 1 σ is marked by the white line. The comparison of the model (stars) and observed main-beam temperatures is shown in the right bottom panel.

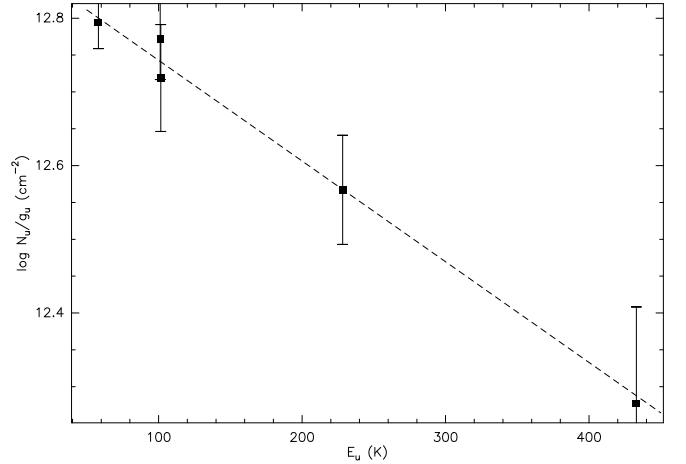


Figure 11. The rotational diagram for HNCO towards the emission peak.

ison with the total gas column density indicates HNCO abundance of $X(\text{HNCO}) \sim 10^{-8}$. This is a rather high value, close to the highest HNCO abundance derived in the survey of massive cores by Zinchenko et al. (2000). However, taking into account the note above about the HNCO lines saturation, this value may need a correction.

In the 350 GHz band we detected many SO_2 lines (Table 2). The corresponding population diagram is shown in Fig. 13. It indicates a range of temperatures. For low-excitation transitions the rotational temperature is 65 ± 11 K. For the high-excitation ones it is 146 ± 16 K. The SO_2 observations were performed at a much lower angular resolution (2 arcsec) than in case of HNCO and apparently include emission from both the hot core and the surrounding cloud. The derived temperatures are

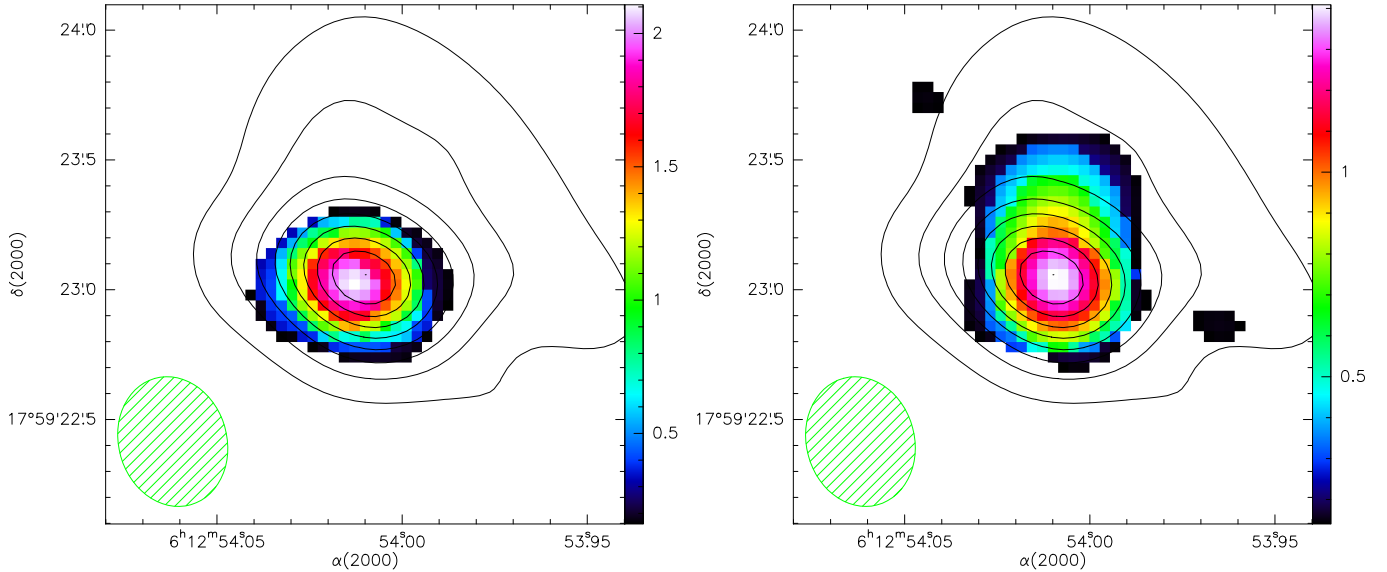


Figure 12. The maps of the integrated intensity of HNCO $J_{K-1} = 10_2 - 9_2$ (left panel) and OCS $J = 18 - 17$ (right panel) transitions (color scale) towards the SMA1 clump. The intensity units are $\text{Jy beam}^{-1} \text{km s}^{-1}$. The beam size is $0''.4$. The contours show the 1.3 mm continuum emission with the same angular resolution. The beam for the molecular maps is shown in the lower left corner of both panels.

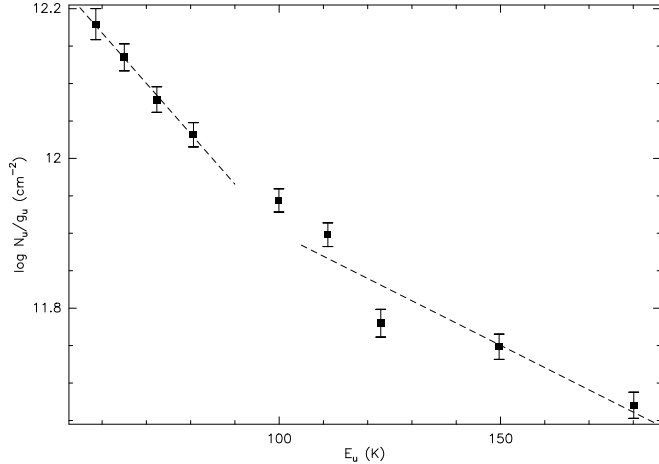


Figure 13. The population diagram for SO_2 at the SMA1 emission peak.

consistent with the other estimates for these components.

Another indicator of the hot environment is the vibrationally excited HCN. We detected the emission in the $v_2 = 1$ state, about 1000 K above the ground state. For the $v_2 = 2$ emission the upper limit is about 5 times lower. Following the analysis presented in e.g. Veach et al. (2013) we obtain an upper limit for the excitation temperature between these states of about 500 K. This is consistent with the other estimates of the gas temperature given above. The critical density for HCN excitation is high ($> 10^{10} \text{ cm}^{-3}$, Veach et al. 2013) which is consistent with our density estimates for the hot gas.

4.1.3. A cold clump in the hot core?

In Fig. 14 we plot maps of the DCN $J = 3 - 2$ and ^{13}CS $J = 5 - 4$ integrated line emission in the SMA1 core. The emission regions are very compact and the emission peak is shifted from the continuum peak which apparently coincides with the YSO location. The projected distance from the continuum peak is roughly 300 AU.

The velocities of the DCN and ^{13}CS emission are prac-

tically the same as those of high excitation lines of other molecules tracing apparently the hot gas. Therefore, most probably the observed DCN emission arises within the disk and since we probably see the disk nearly face-on as discussed above, the physical distance from the center is not much larger than the projected distance. An estimate of the abundances in the LTE approximation gives $X(\text{DCN}) > 10^{-11}$ and $X(^{13}\text{CS}) > 3 \times 10^{-11}$ (assuming the total mass of the clump $< 10 M_\odot$ and temperature of 50–100 K). This is a “normal” value for ^{13}CS while the derived DCN abundance implies a significant deuteration as follows from comparison with typical HCN abundances in massive cores (e.g. Zinchenko et al. 2009). As pointed out in Paper I, recent modelling by Albertsson et al. (2013) shows that DCN/HCN abundance ratio sharply drops at temperatures $\gtrsim 80$ K. It means that temperature of the DCN emitting clump should be rather low, much lower than the temperature of the hot gas in the disk. Another possible explanation, as also discussed in Paper I, can be a very young age of the clump, insufficient to reach the steady-state DCN/HCN abundance ratio, but this looks less probable. In principle, interiors of the accretion disk can be well shielded from an external radiation, probably providing necessary low temperatures. In any case this clump deserves further investigation in order to clarify its properties and nature. It is worth mentioning that the mass of this clump cannot be lower than $\sim 1 M_\odot$, otherwise the inferred ^{13}CS abundance would be unrealistically high. The virial mass we estimate about the same, hence the clump can be gravitationally bound.

4.2. SMA2

As in case of the SMA1 the spectral slope for the continuum emission in the frequency range 284–350 GHz is too low (~ 1.3), which is probably caused by a higher flux loss at higher frequencies. With the SMA at sub-arcsecond resolution we detected a compact component in continuum emission of about the same size as in the SMA1. However, no high-excitation molecular lines

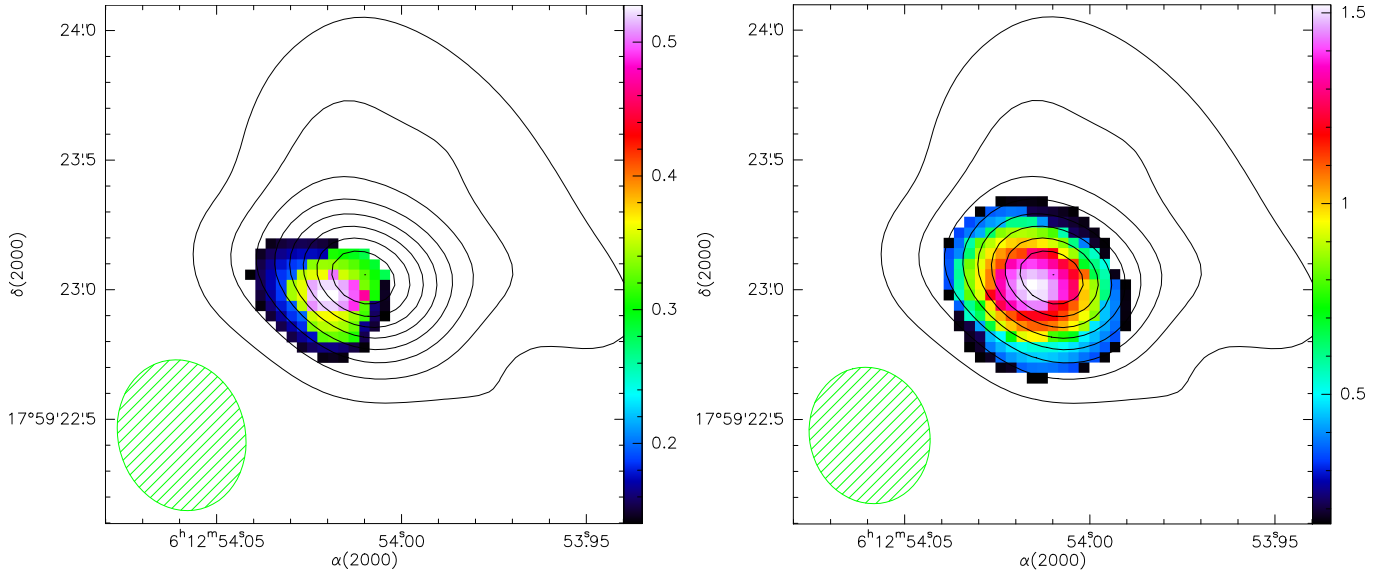


Figure 14. The maps of the integrated intensity of the DCN $J = 3-2$ (left panel) and $^{13}\text{CS } J = 5-4$ (right panel) transitions (color scale) towards the SMA1 clump. The intensity units are $\text{Jy beam}^{-1} \text{ km s}^{-1}$. The beam size is $0''.4$. The contours show the 1.3 mm continuum emission with the same angular resolution. The beam for the molecular maps is shown in the lower left corner of both panels.

could be detected in this area. In Paper I we derived the temperature of the SMA2 clump ~ 40 K. Now with the extended data set, from the methanol excitation analysis (Sect. 3.1.1) we found the 1σ confidence interval for temperature of 40–80 K. The best estimate of the methanol relative abundance is $X(\text{CH}_3\text{OH}) \sim 10^{-8}$. These estimates are obtained at the 2 arcsec scale. It cannot be excluded that the temperature of the compact structure observed in the very extended configuration is somewhat higher. However it cannot be much higher since there is no sign of a higher temperature component in the molecular data. Assuming the temperature of 50 K we obtain the mass of the compact core $\sim 0.2 M_\odot$.

To the west from the SMA2 there is an area of molecular emission without continuum counterpart in the SMA data, observed earlier in the N_2H^+ , NH_3 and several CH_3OH lines (Paper I and Wang et al. 2011). Our new methanol data analysis indicates the temperature in the range 25–65 K, density $n(\text{H}_2)$ in the range 6.3×10^4 – 2.5×10^6 , $X(\text{CH}_3\text{OH}) \sim 10^{-7}$. Some of the methanol transitions are inverted in the model and can be masing. These high gas densities and rather high methanol abundances at relatively low temperatures can be explained by the influence of shock.

4.3. SMA3

In Paper I we did not detect this component which coincides with the near-infrared source NIRS 1 (Tamura et al. 1991) and is identified as a massive disk candidate by NIR polarization observations (Jiang et al. 2008). However, Simpson et al. (2009) argued that these measurements could be affected by instrumental effects and there is no real evidence for the “polarization disk” here. At the same time the NIR measurements indicate a possible outflow related to this object. A comparison with the measurements by Wang et al. (2011) gives a spectral index of about 3.3 in the frequency range 225–350 GHz, consistent with the optically thin dust emission. Wang et al. (2011) estimated mass of this clump at about $2 M_\odot$. At sub-arcsecond resolution we do not see any continuum

(Fig. 1) or molecular emission at this position.

4.4. SMA4

This clump was first detected in Paper I. It shows a weak continuum and spectral line emission in several molecular transitions. The measured continuum flux density at 350 GHz is practically the same as at 284 GHz which also implies a much higher flux loss at the higher frequency. The temperature derived from our new methanol data analysis is about 45 K, higher than estimated in Paper I from ammonia data. However the ammonia emission here is very weak and the uncertainties are high. Some methanol transitions are inverted in the model. The influence of shock is also probable.

5. MORPHOLOGY AND PROPERTIES OF THE OUTFLOWS

In the S255IR area high velocity emission is detected in lines of CO, SiO and several high density tracers including HCN, HCO^+ and CS. In Figs. 15,16 we present channel maps of the CO $J = 3-2$ emission in the blue and red line wings, respectively. The maps of the integrated line wing emission (Fig. 17) show that the CO high velocity emission observed with the SMA looks like a highly collimated bipolar outflow originating near SMA2. There is another more compact component near SMA1.

On the other hand the bipolar outflow observed in HCN and HCO^+ is apparently associated with SMA1 while is parallel to the CO flow (Fig. 17). It is apparently associated with the jet observed in particular in the Fe II emission which is also plotted in this figure. It is worth mentioning that the extent of the jet is much smaller than the extent of the outflow seen in CO, although their orientations coincide.

The SMA data alone hint at two parallel outflows with different origins. However single-dish CO(3–2) observations with the IRAM 30m telescope show a different picture. Here we see a wider outflow clearly originating at SMA1 (Fig. 18). While the emission peaks coincide in the SMA and 30m maps, near the driving source the CO emission measured with the SMA traces only the north-

Table 8
Physical parameters derived from the CH₃OH data obtained in the compact configuration (HPBW $\approx 3''$). The 1σ confidence intervals are indicated in the parentheses.

Object	T_{kin} (K)	$N_{\text{CH}_3\text{OH}}/\Delta V$ ($10^{12} \text{ cm}^{-3} \text{ s}$)	n_{H_2} (cm^{-3})	beam filling factor (%)	$N_{\text{CH}_3\text{OH}}/N_{\text{H}_2}$
SMA2	50 (40–80)	2.0 (1.8–3.5)	6.3×10^6 ($\leq 10^8$)	99.3 (≥ 84)	10^{-8} ($\geq 10^{-8}$)
SMA2-W	40 (25–65)	3.2 (2.2–4.5)	1.0×10^6 (6.3×10^4 – 2.5×10^6)	64.0 (63–70)	10^{-7} ($\geq 10^{-8}$)
SMA4	45 (30–90)	3.6 (0.8–7.9)	5.6×10^4 (10^3 – 6.3×10^5)	99.9 (≥ 20)	10^{-7} (10^{-6} – 10^{-9})

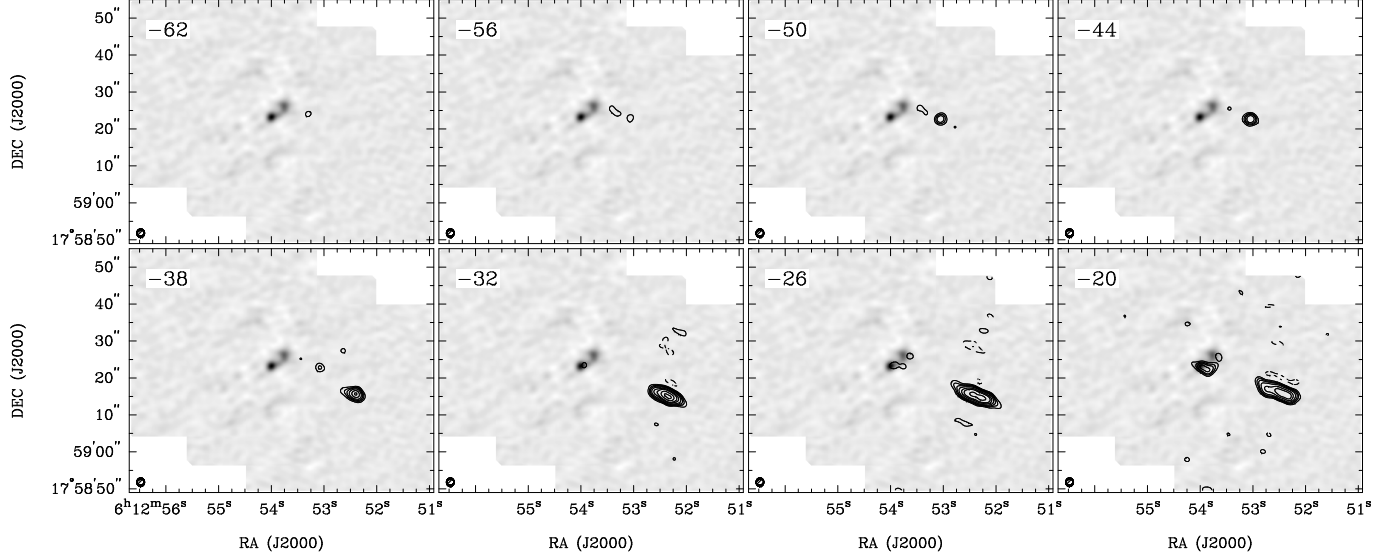


Figure 15. Channel maps of the CO blue wing emission in the S255IR. The numbers in the upper left corner indicate the channel velocity in km s^{-1} . The dashed contours show negative features due to the missing flux. The contour levels are $(-3, 3, 5, 7, 10, 15, 20, 30, 40) \times 100 \text{ mJy beam}^{-1}$. The SMA beam is shown in the lower left corner of each panel.

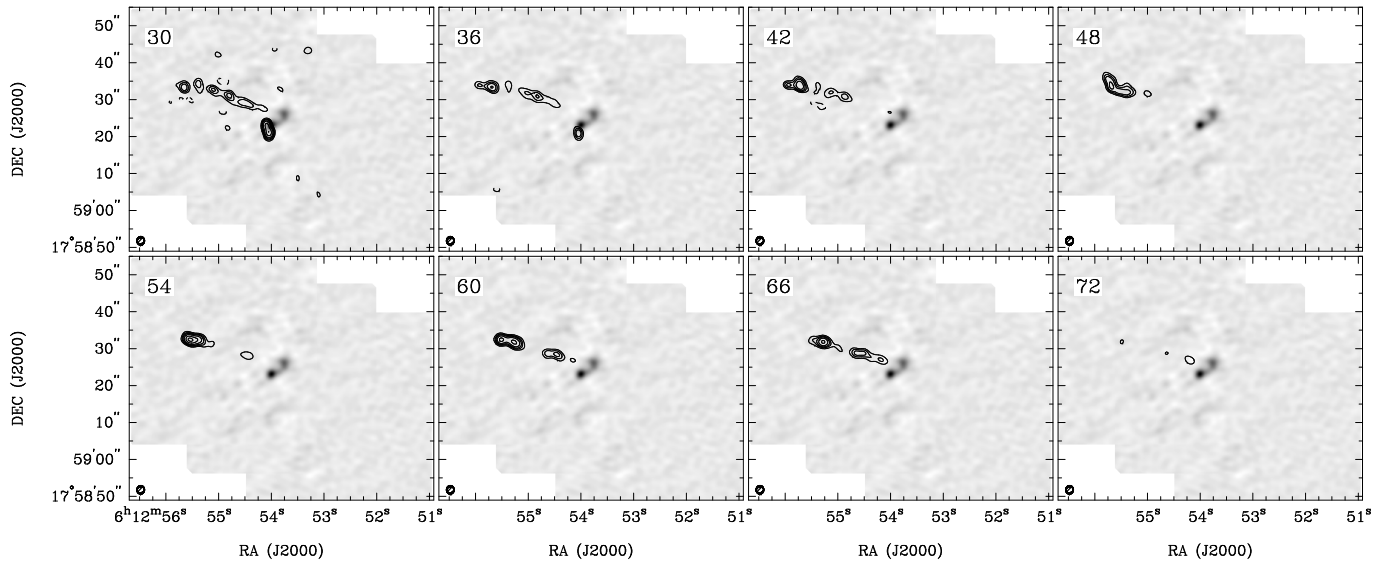


Figure 16. Channel maps of the CO red wing emission in the S255IR. The numbers in the upper left corner indicate the channel velocity in km s^{-1} . The dashed contours show negative features due to the missing flux. The contour levels are $(-3, 3, 5, 7, 10, 15, 20, 30, 40) \times 100 \text{ mJy beam}^{-1}$. The SMA beam is shown in the lower left corner of each panel.

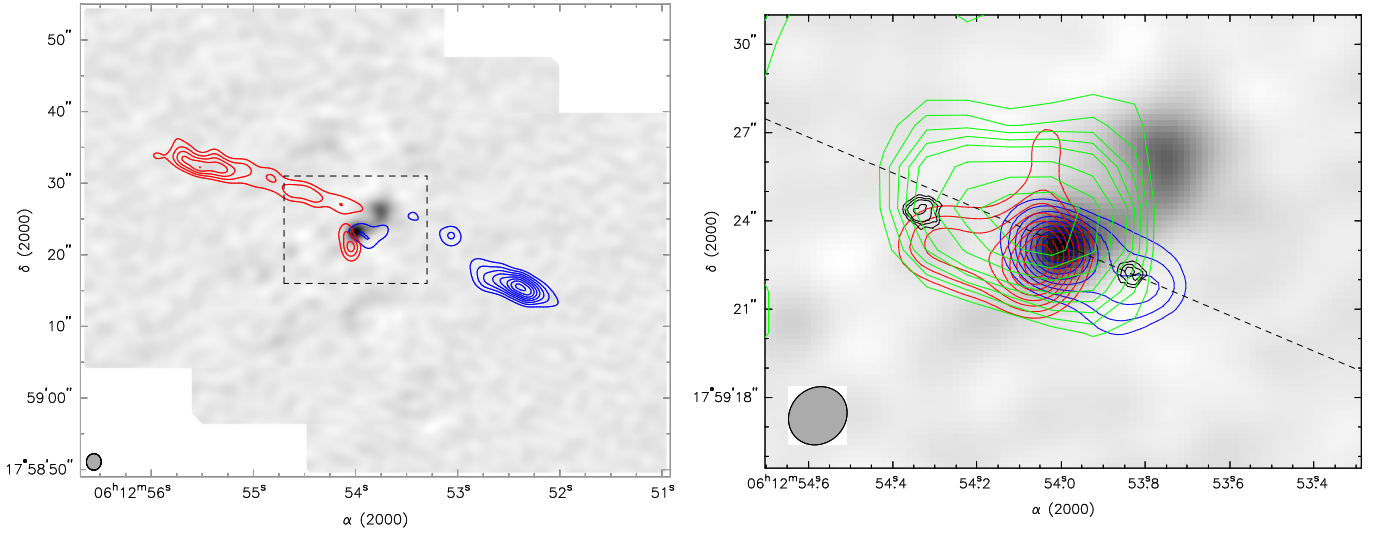


Figure 17. Left panel: maps of the CO(3-2) high velocity emission as observed with the SMA (blue and red contours) in the S255IR area overlaid on the continuum image at 0.8 mm. The SMA1 and SMA2 continuum clumps are marked. The velocity intervals are from -63 km s^{-1} to -13 km s^{-1} for the blue wing and from 25 km s^{-1} to 75 km s^{-1} for the red wing. The dashed rectangle indicates the area shown in the right panel. Right panel: maps of the HCO⁺(4-3) high velocity emission (blue and red contours) in the S255IR area overlaid on the continuum image at 0.8 mm. The velocity intervals are from -19 km s^{-1} to 3 km s^{-1} for the blue wing and from 11 km s^{-1} to 27 km s^{-1} for the red wing. The black contours show the Fe II emission (Wang et al. 2011). The map of the 15 GHz continuum emission (from the VLA archival data, the angular resolution is about 4 arcsec) is plotted with green contours. The dashed line indicates the jet axis (PA = 67°) as in Fig. 5. The SMA beam is shown in the lower left corner of both panels.

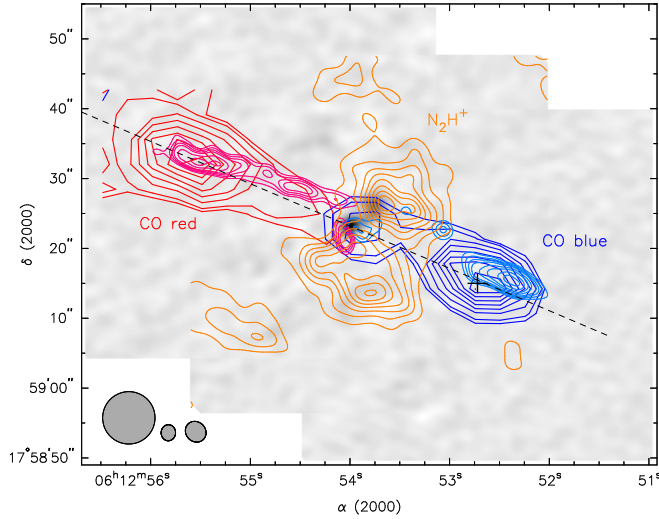


Figure 18. Maps of the CO(3-2) high velocity emission as observed with the IRAM 30m telescope (blue and red thick contours) in the S255IR area overlaid on the continuum image at 0.8 mm. The thin contours show the SMA maps from Fig. 17. The dashed line indicates the axis of the position-velocity cut (PA = 67°). The orange contours show the N_2H^+ (3-2) integrated line emission obtained by combining the SMA and 30m data. The cross marks the position of the high velocity dense clump (Sect. 5.1). The 30m beam and the SMA beams for the CO and N_2H^+ observations, respectively, are shown in the lower left corner (from left to right).

ern edge of the outflow. This shows that the SMA map gives a distorted picture and in reality we have here a wider angle outflow originating at the SMA1.

Apparently this means that this northern edge of the outflow contains a relatively bright component with a characteristic scale comparable to the SMA beam. The southern edge of the outflow near the driving source would be more diffuse and resolved out by the SMA. Most probably this implies that the CO emission is formed in a compressed layer surrounding the outflow cavity. For some (unclear) reason in the northern part this layer is more pronounced. It is worth mentioning that the brightest peaks of the high velocity CO emission practically coincide in the SMA and 30m maps and also coincide with spots of molecular hydrogen emission (Wang et al. 2011) which probably indicate bow shocks. Basic physical parameters of the outflow were estimated by Wang et al. (2011) from their CO(2-1) data. Our new data are consistent with these estimates.

The position-velocity (P-V) diagram for the outflow along the cut indicated in Fig. 18, constructed from the 30m data, is shown in the left panel of Fig. 19. The gap at $V_{\text{LSR}} \sim 24 \text{ km s}^{-1}$ is caused by the emission at the reference offset position mentioned above. In the right panel we present the P-V diagram obtained from the SMA CO(3-2) data. The main features of these diagrams coincide. They show non-monotonic dependence of the velocity on offset, which hints at two outflow components at different distances from the driving source. These P-V diagrams are somewhat different from that presented by Wang et al. (2011). However Wang et al. (2011) plotted this diagram for a different cut, with the position angle of 75°, which makes the direct comparison irrelevant.

In Fig. 20 we plot the P-V diagram for the HCO^+ (4-3) emission as observed with the SMA, along with the part of the CO(3-2) P-V diagram for the same intervals

of the offset and velocity. The diagrams are very similar, which means that both molecules trace apparently the same gas.

5.1. Dense high velocity clump

Our data show a strong, compact blue-shifted CS and HCN emission close to the peak of the CO blue-shifted line wing emission. The peak of this CS and HCN emission is marked by cross in Fig. 18. The CO(3-2), CO(2-1), HCN(4-3), CS(7-6), HCO^+ (4-3) and N_2H^+ (3-2) spectra towards this position are presented in Fig. 21.

One can see rather strong and broad HCN and CS lines at a central velocity of about -5 km s^{-1} . There is a hint of wings in these lines extending to about -20 km s^{-1} . The peak of the CO emission, especially in the higher $J = 3 - 2$ transition is observed at more negative velocities. There is no detectable HCO^+ (4-3), N_2H^+ (3-2), CH_3CN and continuum emission (for N_2H^+ and CH_3CN we use the data from Paper I).

The spatial distribution of the CS(7-6) and CO(3-2) emission integrated in the velocity ranges $-13...+1 \text{ km s}^{-1}$ and $-19...+1 \text{ km s}^{-1}$, respectively, is shown in Fig. 22. The HCN distribution is very similar to that of CS. The deconvolved size of the CS emitting clump is about $1''.1 \times 0''.3$ which corresponds to $1800 \text{ AU} \times 500 \text{ AU}$. It is apparently located at the head of the stream observed in CO, almost exactly at the jet axis shown in Fig. 18.

At the velocity of the CS and HCN emission peak, the brightness temperatures in the CO(3-2), CO(2-1) and HCN(4-3) lines are practically the same. The frequencies of the CO(3-2), HCN(4-3) and CS(7-6) lines are close to each other and beam parameters for them should be similar, too. However, the comparison with the CO(2-1) is complicated by the significantly different frequencies.

The CO(3-2) line is most probably saturated. Then the HCN(4-3) line should be saturated, too. The CS line is weaker implying either a relatively lower optical depth (but close to unity anyway) or a smaller size of the emission region. A simple modeling using e.g. RADEX (van der Tak et al. 2007) shows that the column densities of HCN and CS required to explain such optical depths are $\gtrsim 10^{15} \text{ cm}^{-2}$. The relative abundances of these molecules are $\leq 10^{-8}$. Therefore the total gas column density in the clump is $\gtrsim 10^{23} \text{ cm}^{-2}$. Then, using the size estimated above we obtain the gas density $n \gtrsim 3 \times 10^6 \text{ cm}^{-3}$. This estimate is consistent with the observations of the HCN and CS lines which require at least such densities for excitation.

The large HCN and CS line widths indicate that the clump is gravitationally unbound. The virial mass of this clump estimated in the usual way (e.g. Zinchenko et al. 1994) is $M_{\text{vir}} \sim 30 M_{\odot}$. At the same time, the non-detection of dust emission implies an upper limit for mass orders of magnitudes lower. Therefore, the clump represents a transient entity.

It is worth mentioning the non-detection of HCO^+ and N_2H^+ emission. Both molecules can be destroyed by dissociative recombination (e.g. Zinchenko et al. 2009). Therefore their absence can indicate an enhanced ionization in the dense clump.

5.2. Ionized gas

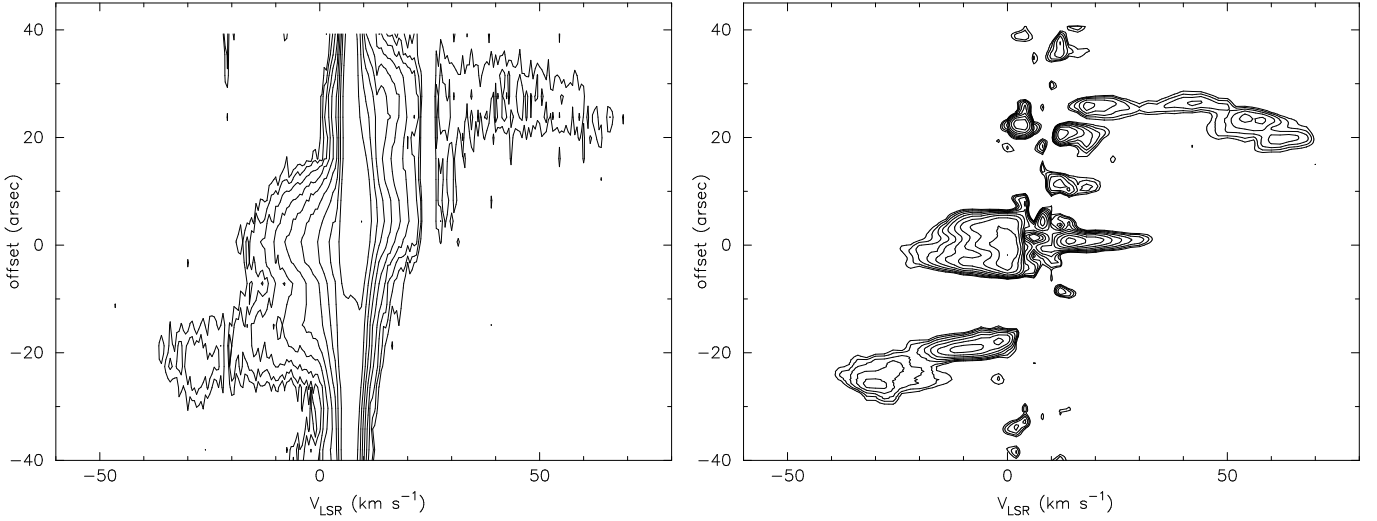


Figure 19. Left panel: the position-velocity map for the CO(3–2) emission as observed with the IRAM 30m telescope along the cut indicated in Fig. 18. The contour levels are on logarithmic scale from 0.4 K to 31.5 K. The gap at $V_{\text{LSR}} \sim 24 \text{ km s}^{-1}$ is caused by the emission at the reference offset position mentioned above. Right panel: the position-velocity map for the CO(3–2) emission as observed with the SMA along the same cut. The contour levels are on logarithmic scale from 0.5 to 11.5 Jy beam^{-1} .

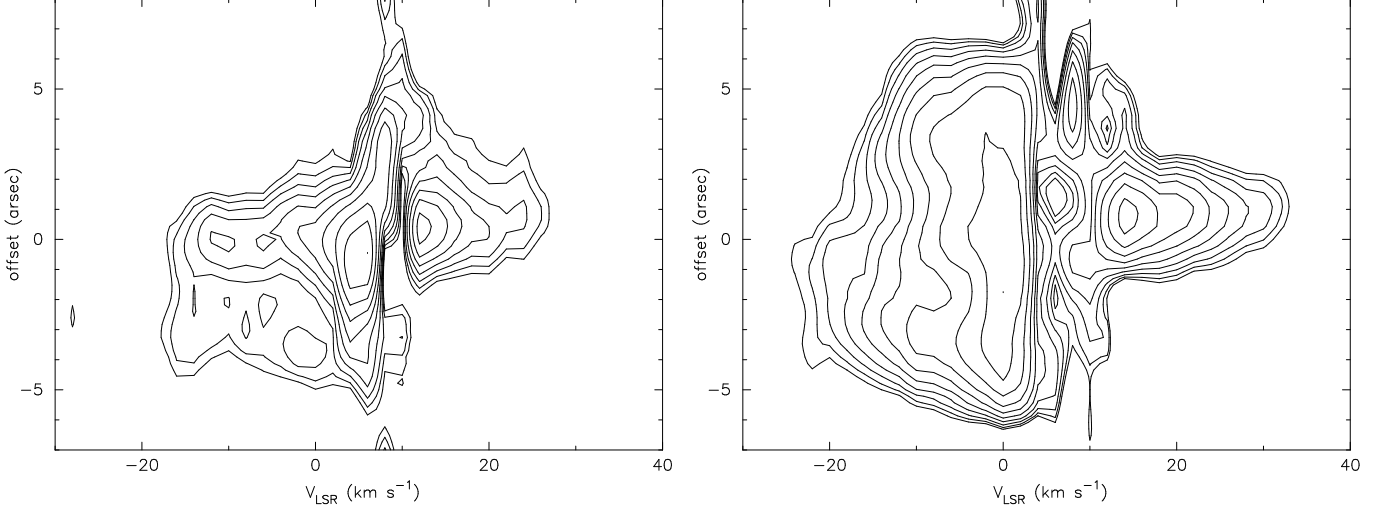


Figure 20. Left panel: the position-velocity map for the $\text{HCO}^+(4-3)$ emission as observed with the SMA along the cut indicated in Fig. 17. The contour levels are on logarithmic scale from 0.4 to 7.6 Jy beam^{-1} . Right panel: a part of the position-velocity map for the CO(3–2) emission measured by the SMA from Fig. 19 for the same intervals of the offset and velocity as in the left panel.

In Fig. 17 we plot the map of the 15 GHz continuum emission near the SMA1/SMA2 clumps (from the VLA archival data, the angular resolution is about 4 arcsec) which shows the distribution of the ionized gas in this area. This ionized component seems to be associated with the jet traced in the Fe II emission. The GMRT map at 1280 MHz looks similar but there is a significant positional uncertainty in the GMRT data (Paper I). Properties of the continuum source were estimated in Paper I and by Ojha et al. (2011). The emission measure is $EM \sim (1 - 2.5) \times 10^7 \text{ pc cm}^{-6}$. Taking into account the observed size of the continuum source, the electron density is $n \sim 3 \times 10^4 \text{ cm}^{-3}$.

6. SURROUNDINGS

The surroundings of the SMA1/SMA2 clumps and high velocity outflow are traced in several molecular lines. One of the most informative is the $\text{N}_2\text{H}^+(3-2)$ transition observed with both SMA and IRAM-30m telescope. The

combined map of the $\text{N}_2\text{H}^+(3-2)$ emission is presented in Fig. 18. It shows an absence of N_2H^+ in the hot core, in accordance with our previous findings (Paper I). The overall morphology of the N_2H^+ emission suggests that it originates in an envelope around the central cores and the outflow lobes.

The distribution of the $\text{SiO}(5-4)$ emission is different (Fig. 23). It peaks near the SMA1 core. There is also a feature in the area of the blue outflow lobe which may be associated with the N_2H^+ emission. The $\text{CS}(7-6)$ distribution (right panel in Fig. 23) seems to be the most uniform one. It shows a rather smooth, almost spherical halo around the SMA1 and SMA2 cores. There is no sign of the outflow influence on the CS distribution. One may suspect that the optical depth in the CS line is too high and we see only the outer regions of the core. However the SMA1 and SMA2 clumps are well resolved in this map which makes such explanation less probable. Then, the total gas distribution is apparently not significantly

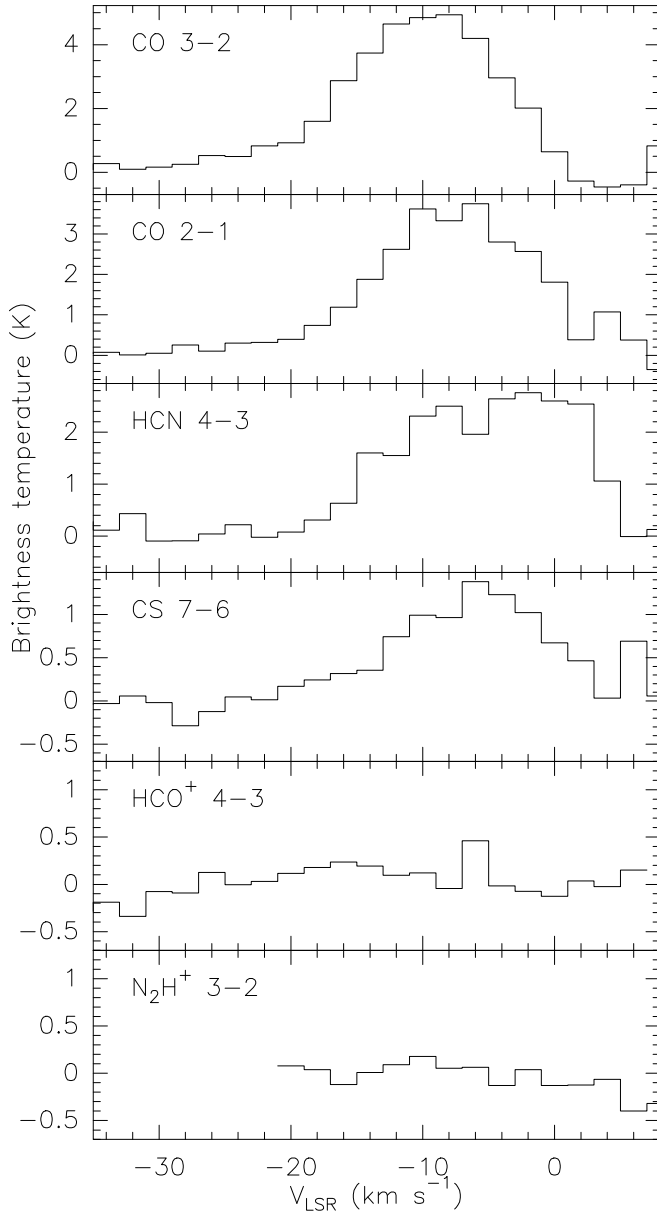


Figure 21. The CO(3-2), CO(2-1), HCN(4-3), CS(7-6), HCO⁺(4-3) and N₂H⁺(3-2) spectra towards the position marked by cross in Fig. 18.

affected, too.

7. DISCUSSION

The main goal of this study is the characterization of the outflow and probable accretion disk associated with the massive YSO in the S255IR clump. The data presented in the previous sections shed new light on this system.

Concerning the outflow, one of the main findings is that the SMA interferometric data alone give a rather distorted picture. They hint at two highly collimated parallel outflows with different centers of origin. However, this impression is apparently caused by a significant flux loss in the interferometric measurements. The single-dish CO observations clearly show a single less collimated outflow originating at the SMA1 core. The CO emission retrieved by the SMA near the driving source originates apparently from the northern wall of the out-

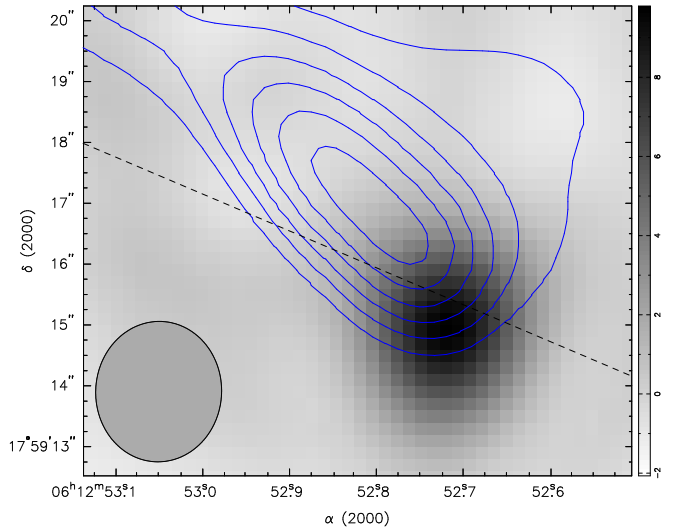


Figure 22. The map of CO(3-2) emission in the velocity range $-19...+1$ km s⁻¹ (contours) overlaid on image of CS(7-6) emission in the velocity range $-13...+1$ km s⁻¹ (grey scale). The intensity units for the image are Jy beam⁻¹ km s⁻¹. The contour levels are (3, 5, 7, 9, 11, 13) × 5 Jy beam⁻¹ km s⁻¹. The SMA beam is shown in the lower left corner.

flow cavity. This means that this part of the wall is rather thin and bright. The absence of a noticeable CO emission at the opposite side of the wall implies a more diffuse distribution of the emission here, probably due to the density structure of the surrounding medium.

The question arises of how common is this effect in the interferometric studies of outflows. We can easily imagine a situation when an interferometric image will show multiple outflows from a single driving source, while in fact there is a single wide-angle outflow.

The observed P-V diagrams for the outflow (Figs. 19,20) most probably indicate periodic ejections from the driving source. Two events can be traced in the data. They apparently created jet knots at different distances from the central star. The older one is responsible for the extended CO outflow. The peaks of the CO emission coincide with bright H₂ emission spots (Wang et al. 2011) which probably indicate bow shocks at the heads of the jets. The next ejection event created other bow shocks which are seen in particular in the Fe II emission (Fig. 17). This later ejection entrains dense molecular gas observed in the wings of the HCO⁺, HCN and CS lines. It is also traced in the CO emission as can be seen in the CO position-velocity diagram (Figs. 19,20). Another manifestation of this activity is apparently the dense high velocity clump (Sect. 5.1), which most probably represents dense gas at the head of bow shock. All the jet knots lay practically on a straight line. Therefore the orientation of the jet does not change with time significantly. The age of the first, extended outflow was estimated of about 7000 years by Wang et al. (2011). Assuming the same ejection velocities for the two events and comparing distances of the bow shocks from the driving source we can conclude that the second ejection happened about 1000 years ago. Therefore the time interval between the ejection events is about 6000 years (the age estimates were done under the usual assumption of an inclination angle for the jet of 45°).

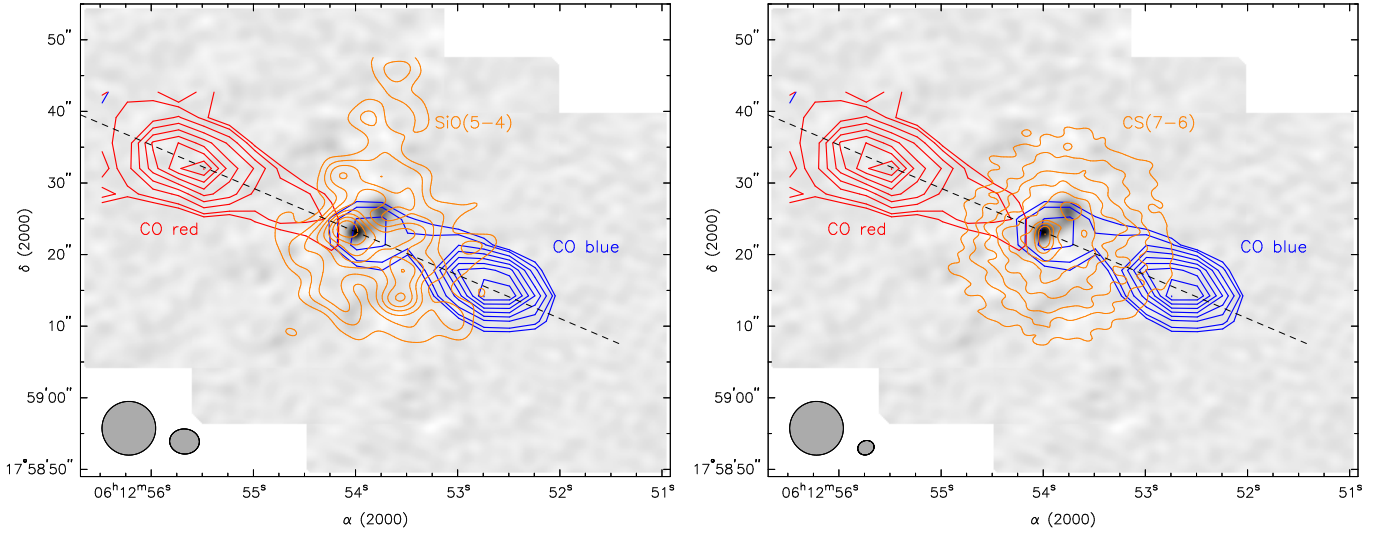


Figure 23. Left panel: the maps of the SiO(5–4) (left panel) and CS(7–6) (right panel) integrated line emission obtained by combining the SMA and 30m data (orange contours) overlaid on the continuum image at 0.8 mm. The maps of the CO(3–2) high velocity emission as observed with the IRAM 30m telescope (blue and red thick contours) from Fig. 18 are also shown. The beams for the IRAM-30m telescope and for the combined maps are shown in the lower left corner of each panel.

Several entrainment mechanisms are usually discussed for molecular outflows (e.g. Arce et al. 2007; Frank et al. 2014). In our case the most probable one is the jet bow-shock model (e.g. Raga & Cabrit 1993). The main argument in favor of this model is the obvious presence of several bow shocks (traced in the H_2 and Fe II emission) clearly associated with the high velocity molecular gas. This model is also consistent with the observed outflow morphology and kinematics. The shape of the P–V diagram differs from the frequently observed “Hubble law” and shows a range of velocities at the largest distances from the driving source. A similar shape was observed in some other outflows which are apparently driven by bow shocks and is expected in the theoretical models (e.g. Lee et al. 2000).

The jet is apparently launched from the accretion disk around the central massive young star. As mentioned above, there is a chain of water masers along the jet. For several water maser spots shown in Fig. 5, proper motions have been measured (Goddi et al. 2007). The velocities (from $\sim 10 \text{ km s}^{-1}$ to $\sim 30 \text{ km s}^{-1}$ at the distance of 1.6 kpc) are mostly perpendicular to the jet axis with outward components in some cases. The maser velocity pattern is consistent with clockwise rotation around the core center. Velocities of the masers closest to the center imply dynamical mass of the order of $20 M_\odot$. The mass of the central star is estimated to be $27 M_\odot$ (Ojha et al. 2011) assuming the distance of 2.5 kpc. At the distance of 1.6 kpc the mass of the star would be $23.5 \pm 3.6 M_\odot$. This estimate is based on the unpublished value of the star luminosity of $(6.8 \pm 2.8) \times 10^4 L_\odot$ (for the distance of 1.6 kpc). Now we reconsidered the star SED by including data at millimeter wavelengths from Zinchenko et al. (2009). This results in the luminosity of $(3.5 \pm 0.3) \times 10^4 L_\odot$ and mass of $20 \pm 2 M_\odot$. It is worth mentioning that Pashchenko et al. (2003) estimated the mass of the central star to be (6–7) M_\odot from their analysis of water masers variability. However, they employed a systemic velocity of 8.3 km s^{-1} which contradicts our findings which clearly show the systemic velocity to be about 4.8 km s^{-1} . In the following we will take

the mass of $20 M_\odot$ as the most probable value. This is sufficient to explain velocities of the masers closest to the star. However maser spots located at larger distances from the center have similar velocities and imply a much larger central mass of the order of $100 M_\odot$. This value is inconsistent with all other estimates. The corresponding mean density would be unrealistically high. This means that we probably need another explanation for the maser velocities. Rather speculative, it can be jet rotation. Rapid rotation of protostellar jets is expected in theoretical models (e.g. Pudritz et al. 2007) and was indeed observed in some cases (Bacciotti et al. 2002).

The water masers are thought to be excited by interaction of the jet with the surrounding medium. The fact that they are moving in one direction on each side of the central star implies some asymmetry in the system. There may be some misalignment between the jet and the rotation axis of the material in the outer parts of the clump (apparently, in the axially-symmetric case the observed maser movements would be symmetric relative the axis). It can be that in the inner part the orientation of the disk plane is different. However, the difference cannot be large. We see also other indications of the jet interaction with the surrounding medium, in particular, increased line widths along the jet.

Fig. 5 shows that the water maser condensations are shifted from the jet axis in direction of their proper motion. This projected shift is of the order of 200 AU. At the velocities mentioned above, the maser condensations would travel this distance in about 30–100 years. From this consideration it looks probable that the event created these masers happened quite recently.

The disk is apparently strongly fragmented as follows from the derived beam filling factor (~ 0.2) for CH_3CN and CH_3OH . The mean gas density in the disk is about $6 \times 10^8 \text{ cm}^{-3}$. The density of the fragments should be much higher. Observations of vibrationally excited HCN indicate densities $> 10^{10} \text{ cm}^{-3}$ which is consistent with this picture.

The derived mass of the hot gas ($\sim 0.3 M_\odot$) is by an order of magnitude insufficient to gravitationally bound

the core. The virial mass estimated in the usual way (e.g. Zinchenko et al. 1994) from the line width is about $7 M_{\odot}$. There can be also some amount of cold material in the disk, as follows from the DCN observations. However, the total mass of the disk is apparently much lower than mass of the central star which is estimated of about $20 M_{\odot}$ (see above). Since the disk mass is significantly lower than the star mass, the disk is probably not self-gravitating and we may expect Keplerian rotation. Unfortunately the achieved angular resolution is not sufficient to measure reliably the disk rotation curve.

For a central mass of $20 M_{\odot}$ the inclination angle of the disk (derived from comparison of the observed rotation line-of-sight velocity with the expected velocity for this mass) should be small, about 25° (Fig. 6), i.e. the disk is seen almost face-on. This is consistent with our maps which do not show a significant elongation of this object. On the other hand this conclusion looks somewhat suspicious because of the well-collimated appearance of the molecular outflow. Observations at a higher angular resolution are needed to clarify the structure and kinematics of this object.

The temperature of the hot gas derived from the CH_3CN , CH_3OH and SO_2 observations is about 130–180 K. A similar estimate for the temperature of the hot component was obtained by us many years ago from the analysis of the IRAS data (Zinchenko et al. 1990). The HNC rotational temperature is somewhat higher, about 320 K. However, as mentioned above, this value probably represents an upper limit to the excitation temperature. In addition, the HNC excitation can be influenced by the FIR radiation. The HNC excitation in massive cores was discussed by Zinchenko et al. (2000). That analysis shows that in the present case collisional excitation can be effective. The critical density for excitation of the $K_{-1} = 3$ ladder is of the order of 10^{10} cm^{-3} . Such density is quite possible in the SMA1 core as follows from the estimates above. However the radiative excitation by FIR emission via the b -type transitions cannot be excluded, too. With the column density of $N(\text{H}_2) \sim 3 \times 10^{24} \text{ cm}^{-2}$ the dust will be optically thick at these frequencies creating a sufficiently strong radiation field. The HNC excitation especially in the higher K_{-1} ladders may reflect the effective temperature of this field.

The highest temperature of the observed molecular material is about 300 K. Taking the source luminosity to be about $3.5 \times 10^4 L_{\odot}$ (see above) this value corresponds to the dust equilibrium temperature at the distance of 200–300 AU from the star. Since we do not see warmer molecular gas, no dust should be present within this radius in case of no shielding. However this radius is comparable to the observed size of the core and we do not see any central hole in the molecular distribution. It is then possible that shielded molecular clumps are distributed at smaller radii.

In this respect an interesting feature of our observations is the apparently relatively cold and rather massive clump with a strong DCN emission. It may be gravitationally bound and the mass of the clump is sufficiently high to consider it as a possible low-mass protostar.

Concerning the surroundings of the SMA1 clump, we see that the outflow strongly affects the chemical composition of the medium. The N_2H^+ molecules are destroyed

along the outflow. The SiO distribution seems to be also significantly affected. At the same time there is no noticeable influence on the CS distribution. The density structure is probably not affected, too. As mentioned above (Sect. 4.2,4.4) the nearby clumps are probably influenced by shocks which are apparently associated with this outflow.

8. CONCLUSIONS

We presented the results of our observations of the S255IR area with the SMA at 1.3 mm in the very extended configuration and at 0.8 mm in the compact configuration as well as with the IRAM-30m at 0.8 mm. The best achieved angular resolution is about 0.4 arcsec. The dust continuum emission and several tens of molecular spectral lines are observed. The majority of the lines is detected only towards the S255IR-SMA1 clump. In summary, our main findings are the following:

1. The S255IR-SMA1 clump represents apparently a rotating structure (probably a disk) around the young massive star. The achieved angular resolution is still insufficient to establish the character (Keplerian or non-Keplerian) of the rotation. The temperature of the molecular gas reaches 130–180 K. The size of the clump is about 500 AU. It is apparently strongly fragmented as follows from the derived small (~ 0.2) beam filling factors for various molecules. The mean gas density is about $6 \times 10^8 \text{ cm}^{-3}$. The density of the fragments should be much higher which is confirmed by observations of HNC and vibrationally excited HCN. The mass of the hot gas is $\sim 0.3 M_{\odot}$ and the total mass of the clump is significantly lower than the mass of the central star (about $20 M_{\odot}$). The inclination angle of the disk (derived from comparison of the observed rotation line-of-sight velocity with the expected rotation velocity for this mass) should be small, about 25° .

2. We detected a strong DCN(3–2) emission near the center of the SMA1 clump. Most probably it indicates the presence of a rather large amount ($\gtrsim 1 M_{\odot}$) of cold (≤ 80 K) material. This cold clump can be gravitationally bound.

3. High velocity emission is observed in the CO line as well as in lines of high density tracers HCN, HCO^+ , CS and other molecules. The CO outflow is much more extended than that observed in the lines of high density tracers. Its morphology obtained from combination of the SMA and IRAM-30m data is significantly different from that derived from the SMA data alone. The CO emission detected with the SMA traces only one boundary of the outflow and leads to a rather distorted picture of the outflow structure. The velocity of the CO outflow reaches $\sim 60 \text{ km s}^{-1}$.

4. The outflow is most probably driven by the jet bow shock mechanism. The available data indicate at least two major ejection events with a time interval of several thousand years between them. The direction of the ejections does not change with time. The high velocity emission in the lines of high density tracers is associated with the peaks of the Fe II emission related to the bow shocks caused by rather recent ejections from the SMA1.

We detected a dense high velocity clump associated apparently with one of the bow shocks. It shows a strong emission in the HCN(4–3) and CS(7–6) lines. At the same time there is no detectable HCO^+ (4–3) or N_2H^+ (3–

2) emission which can be probably explained by enhanced ionization.

5. The proper motions of the water masers excited along the jet imply some misalignment of the jet with the rotation axis of the material in the outer parts of the clump. It can be that the orientation of the disk in the inner and outer parts is somewhat different. However, the difference cannot be large.

6. The outflow strongly affects the chemical composition of the surrounding medium. The N_2H^+ molecules are destroyed along the outflow. The SiO distribution seems to be also significantly affected. At the same time there is no sign of the outflow influence on the CS distribution. The total gas distribution is apparently not significantly affected, too.

This work was supported by the Russian Academy of Sciences (Research program No. 17 of the Department of Physical Sciences), Russian Foundation for Basic Research (RFBR), National Science Council (NSC) of Taiwan and Department of Science and Technology (DST) of the Government of India in frameworks of the research grants RFBR 08-02-92001-NSC, RFBR 13-02-92697-Ind, RFBR 15-02-06098, 15-52-45057, NSC 97-2923-M-001-004-MY3, DST-RFBR INT/RUS/RFBR/P-142. A.M.S. was supported by the Russian Science Foundation (grant number 15-12-10017). S.V.S. was supported by the Ministry of Education and Science of the Russian Federation (state task No. 3.1781.2014/K). Y.W. was supported by Swiss National Science Foundation, NSFC 11303097 and 11203081, China. The research is also partly supported by the grant within the agreement No. 02.49.21.0003 between The Ministry of Education and Science of the Russian Federation and Lobachevsky State University of Nizhni Novgorod and by Russian Education and Science Ministry Project 3.1252.2014/k. We are grateful to Elena Trofimova for the help with the line identification and to the anonymous referee for the detailed helpful comments. The research has made use of the SIMBAD database, operated by CDS, Strasbourg, France.

REFERENCES

- Albertsson, T., Semenov, D. A., Vasyunin, A. I., Henning, T., & Herbst, E. 2013, *ApJS*, 207, 27
- Arce, H. G., Shepherd, D., Gueth, F., et al. 2007, *Protostars and Planets V*, 245
- Bacciotti, F., Ray, T. P., Mundt, R., Eisloffel, J., & Solf, J. 2002, *ApJ*, 576, 222
- Beuther, H., Walsh, A. J., & Longmore, S. N. 2009, *ApJS*, 184, 366
- Boucher, D., Burie, J., Bauer, A., Dubrulle, A., & Demaison, J. 1980, *Journal of Physical and Chemical Reference Data*, 9, 659
- Chavarría, L. A., Allen, L. E., Hora, J. L., Brunt, C. M., & Fazio, G. G. 2008, *ApJ*, 682, 445
- Cragg, D. M., Sobolev, A. M., & Godfrey, P. D. 2005, *MNRAS*, 360, 533
- Frank, A., Ray, T. P., Cabrit, S., et al. 2014, *Protostars and Planets VI*, 451
- Goddi, C., Moscadelli, L., Sanna, A., Cesaroni, R., & Minier, V. 2007, *A&A*, 461, 1027
- Howard, E. M., Pipher, J. L., & Forrest, W. J. 1997, *ApJ*, 481, 327
- Itoh, Y., Tamura, M., Suto, H., et al. 2001, *PASJ*, 53, 495
- Jiang, Z., Tamura, M., Hoare, M. G., et al. 2008, *ApJ*, 673, L175
- Lee, C.-F., Mundy, L. G., Reipurth, B., Ostriker, E. C., & Stone, J. M. 2000, *ApJ*, 542, 925
- Miralles, M. P., Salas, L., Cruz-Gonzalez, I., & Kurtz, S. 1997, *ApJ*, 488, 749
- Müller, H. S. P., Schlöder, F., Stutzki, J., & Winnewisser, G. 2005, *Journal of Molecular Structure*, 742, 215
- Müller, H. S. P., Thorwirth, S., Roth, D. A., & Winnewisser, G. 2001, *A&A*, 370, L49
- Ojha, D. K., Samal, M. R., Pandey, A. K., et al. 2011, *ApJ*, 738, 156
- Ossenkopf, V. 1997, *New Astronomy*, 2, 365
- Ossenkopf, V., & Henning, T. 1994, *A&A*, 291, 943
- Pashchenko, M. I., Lekht, E. E., & Tolmachev, A. M. 2003, *Astronomy Letters*, 29, 26
- Pickett, H. M., Poynter, R. L., Cohen, E. A., et al. 1998, *J. Quant. Spec. Radiat. Transf.*, 60, 883
- Pirogov, L. E., & Zinchenko, I. I. 2008, *Astronomy Reports*, 52, 963
- Pirogov, L. E., Zinchenko, I. I., Johansson, L. E. B., & Yang, J. 2012, *Astronomical and Astrophysical Transactions*, 27, 475
- Pudritz, R. E., Ouyed, R., Fendt, C., & Brandenburg, A. 2007, *Protostars and Planets V*, 277
- Raga, A., & Cabrit, S. 1993, *A&A*, 278, 267
- Russeil, D., Adami, C., & Georgelin, Y. M. 2007, *A&A*, 470, 161
- Rygl, K. L. J., Brunthaler, A., Reid, M. J., et al. 2010, *A&A*, 511, A2
- Sault, R. J., Teuben, P. J., & Wright, M. C. H. 1995, in *Astronomical Society of the Pacific Conference Series*, Vol. 77, *Astronomical Data Analysis Software and Systems IV*, ed. R. A. Shaw, H. E. Payne, & J. J. E. Hayes, 433
- Scoville, N. Z., Carlstrom, J. E., Chandler, C. J., et al. 1993, *PASP*, 105, 1482
- Sherwood, W. A., Arnold, E. M., & Schultz, G. V. 1980, in *IAU Symposium*, Vol. 87, *Interstellar Molecules*, ed. B. H. Andrew, 133
- Simpson, J. P., Burton, M. G., Colgan, S. W. J., et al. 2009, *ApJ*, 700, 1488
- Snell, R. L., & Bally, J. 1986, *ApJ*, 303, 683
- Sutton, E. C., Sobolev, A. M., Salii, S. V., et al. 2004, *ApJ*, 609, 231
- Tamura, M., Gatley, I., Joyce, R. R., et al. 1991, *ApJ*, 378, 611
- van der Tak, F. F. S., Black, J. H., Schöier, F. L., Jansen, D. J., & van Dishoeck, E. F. 2007, *A&A*, 468, 627
- Veach, T. J., Groppi, C. E., & Hedden, A. 2013, *ApJ*, 765, L34
- Wang, K.-S., Kuan, Y.-J., Liu, S.-Y., & Charnley, S. B. 2010, *ApJ*, 713, 1192
- Wang, Y., Beuther, H., Bik, A., et al. 2011, *A&A*, 527, A32
- Zinchenko, I., Caselli, P., & Pirogov, L. 2009, *MNRAS*, 395, 2234
- Zinchenko, I., Forsstroem, V., Lapinov, A., & Mattila, K. 1994, *A&A*, 288, 601
- Zinchenko, I., Henkel, C., & Mao, R. Q. 2000, *A&A*, 361, 1079
- Zinchenko, I., Liu, S.-Y., Su, Y.-N., et al. 2012, *ApJ*, 755, 177
- Zinchenko, I. I., Krasilnikov, A. A., Kukina, E. P., Lapinov, A. V., & Pirogov, L. E. 1990, *Soviet Ast.*, 34, 458